



**HAL**  
open science

# Jet instability of suspensions of different shaped particles exhibiting discontinuous shear thickening

M. Meloussi, S. Schaub, A. Cifreio, S. Aguib, P. Kuzhir

► **To cite this version:**

M. Meloussi, S. Schaub, A. Cifreio, S. Aguib, P. Kuzhir. Jet instability of suspensions of different shaped particles exhibiting discontinuous shear thickening. *Journal of Rheology*, 2022, 66 (5), pp.1005-1026. 10.1122/8.0000471 . hal-03880661

**HAL Id: hal-03880661**

**<https://hal.science/hal-03880661>**

Submitted on 1 Dec 2022

**HAL** is a multi-disciplinary open access archive for the deposit and dissemination of scientific research documents, whether they are published or not. The documents may come from teaching and research institutions in France or abroad, or from public or private research centers.

L'archive ouverte pluridisciplinaire **HAL**, est destinée au dépôt et à la diffusion de documents scientifiques de niveau recherche, publiés ou non, émanant des établissements d'enseignement et de recherche français ou étrangers, des laboratoires publics ou privés.

# Jet instability of suspensions of different shaped particles exhibiting discontinuous shear thickening

M. Meloussi, S. Schaub, A. Cifreó, et al.

Citation: *Journal of Rheology* **66**, 1005 (2022); doi: 10.1122/8.0000471

View online: <https://doi.org/10.1122/8.0000471>

View Table of Contents: <https://sor.scitation.org/toc/jor/66/5>

Published by the [The Society of Rheology](#)

---

## ARTICLES YOU MAY BE INTERESTED IN

[Hydrodynamic origin for the suspension viscoelasticity of rough colloids](#)

*Journal of Rheology* **66**, 895 (2022); <https://doi.org/10.1122/8.0000424>

[Granulation and suspension rheology: A unified treatment](#)

*Journal of Rheology* **66**, 853 (2022); <https://doi.org/10.1122/8.0000515>

[Ordered domains in sheared dense suspensions: The link to viscosity and the disruptive effect of friction](#)

*Journal of Rheology* **66**, 1055 (2022); <https://doi.org/10.1122/8.0000453>

[Rheology and microstructure of discontinuous shear thickening suspensions](#)

*Journal of Rheology* **66**, 731 (2022); <https://doi.org/10.1122/8.0000317>

[The Mnemosyne number and the rheology of remembrance](#)

*Journal of Rheology* **66**, 1027 (2022); <https://doi.org/10.1122/8.0000432>


[Determination of the molecular weight distribution of ultrahigh molecular weight polyethylene from solution rheology](#)

*Journal of Rheology* **66**, 1079 (2022); <https://doi.org/10.1122/8.0000502>

---



**True powder rheology**

 **Anton Paar**

[Find out more](#)



# Jet instability of suspensions of different shaped particles exhibiting discontinuous shear thickening

M. Meloussi,<sup>1,2,a)</sup> S. Schaub,<sup>3</sup> A. Ciffo, <sup>2</sup> S. Aguib,<sup>1</sup> and P. Kuzhir<sup>2,b)</sup>

<sup>1</sup>*Dynamic of Engines and Vibroacoustic Laboratory (LDMV), Faculty of Technology, Department of Mechanical Engineering, M'Hamed Bougara University, Boumerdes 35000, Algeria*

<sup>2</sup>*Institute of Physics of Nice, University Côte d'Azur, CNRS UMR 7010, Parc Valrose, 06108 Nice, France*

<sup>3</sup>*Developmental Biology Laboratory (LBDV), Sorbonne University, CNRS, Quai de la Darse, 06234 Villefranche-sur-Mer Cedex, France*

(Received 10 March 2022; final revision received 13 June 2022; published 26 August 2022)

## Abstract

This work is devoted to the detailed study of jet instability occurring in concentrated aqueous mixtures of calcium carbonate (CC) isotropic-shaped particles and rigid polyamide (PA) fibers. These mixtures exhibit very sharp discontinuous shear thickening (DST). The jets were subjected to a free fall under gravitational stretching at a constant flow rate. In the absence of PA fibers, we observed relatively strong lateral oscillations occurring for jet lengths  $L \gtrsim 6$  cm and accompanied by small periodic undulations of the jet diameter. Two-dimensional Direct Fourier Transform analysis reveals approximately linear dispersion relations for propagation of lateral oscillations and diameter undulations with similar wave speeds  $\sim 1$  m/s. This instability is ascribed to complex rheological behavior in an extensional flow above the DST transition. Theoretical modeling reveals abrupt jumps of the tensile stress along the jet likely leading to fluctuation of longitudinal and transverse velocity fields within the jet perceived through jet diameter and centerline undulations. The addition of PA fibers to CC suspension damps lateral oscillations but favors ruptures along the jet. This is tentatively explained by the interplay between growing lower and decreasing upper DST threshold stresses with increasing fiber volume fraction  $\varphi_f$  along with the thinning of the jet diameter down to the size of fiber flocs. Quantitatively, the stabilizing effect of PA fibers is manifested through an abrupt decrease in the lateral drift amplitude at  $\varphi_f \gtrsim 0.75$  vol %. © 2022 The Society of Rheology. <https://doi.org/10.1122/8.0000471>

## I. INTRODUCTION

Liquid jets are encountered both in daily life (water flows out of taps and shower heads) and in many industrial, agricultural, or biomedical applications (jet cutting, liquid injection, cleaning, jet printing, 3D-printing, agricultural irrigation, drug spraying, etc.). Depending on their rheology and surface tension, liquid jets offer a diversity of striking physical phenomena, most often related to surface instabilities. For example, weakly viscous (in theory inviscid) jets are subject to Rayleigh-Plateau and Kelvin-Helmholtz instabilities appearing as a result of capillary forces or tangential velocity jumps at the jet interface. Newtonian viscous jets are subject to coiling instability usually observed with falling honey threads approaching a solid surface. “Beads-on-a-string” structures are observed for jets of flexible polymer solutions as a result of polymer stretching along the flow. Yield stress fluids like toothpaste or mayonnaise exhibit pinching-off when flowing out of a tube. All these and many other kinds of jet behaviors are extensively described in literature from both theoretical and experimental perspectives—see, for instance, an excellent review by Eggers and Villermaux [1]. Surprisingly, jets of discontinuous shear thickening fluids have received much less attention despite spectacular

instabilities observed each time in the beginning of rheological experiments when the fluid is poured into rheometer.

In general, discontinuous shear thickening (DST) transition is an abrupt increase in the fluid viscosity above some critical shear stress [2,3]. This phenomenon usually occurs in concentrated suspensions of Brownian or non-Brownian hard or soft particles and is commonly attributed to transition from lubricated to frictional interparticle contacts under applied critical stress [4–6]. The DST transition has been extensively studied for shear flows, for which flow curves have an S-shape with two stable branches corresponding to positive slopes and an unstable branch with a negative slope. The shear rate exhibits chaotic fluctuations at constant applied shear stress, whose value is situated on the unstable branch, and these fluctuations can be accompanied by particle migration and vorticity banding [7,8]. From the microscopic perspective, the flow oscillations are believed to occur due to periodic formation and failure of particle contact network governed by the interplay between compressive (due to applied stress) and repulsive (electrostatic or steric) forces between particles [9–11]. Changing the particle shape from spheres to fibers preserves the qualitative features of DST transition [12]. In particular, in our previous work, we have studied the rheology of mixtures of polyamide (PA) rigid fibers dispersed in a shear thickening fluid, which is a suspension of isotropic-shaped calcium carbonate (CC) particles dispersed in a Newtonian liquid [13]. It has been shown, among others, that DST transition is very sharp for these

<sup>a)</sup>m.meloussi@univ-boumerdes.dz

<sup>b)</sup>Author to whom correspondence should be addressed; electronic mail: pavel.kuzhir@univ-cotedazur.fr

fluids, and PA fiber addition shifts this transition to lower shear rates  $\dot{\gamma}$  and to higher shear stresses  $\sigma$ . The fiber orientation has been predicted to significantly affect the critical  $\dot{\gamma}_c$  and  $\sigma_c$  values of DST transition through its effect on the viscosity of the CC-PA mixture: random orientation provides higher viscosity and is expected to lead to lower  $\dot{\gamma}_c$  values compared to fibers aligned by the flow. Above the percolation threshold of fibers, the CC-PA mixture exhibits a solid behavior and does not flow at the highest achievable shear stress of a rheometer. This has been ascribed to bridging of neighboring fibers into a solid percolated network through local shear thickening of CC suspension in confined spaces between fibers.

Extensional flows of DST fluids have been studied to a lesser extent. Filament stretching (FiSER) and capillary break-up (CaBER) extensional rheometry was employed in experiments and has shown qualitatively similar behavior to those observed in shear rheometry: a nearly constant extensional viscosity at low strain rates followed by an abrupt increase above a critical strain rate [14,15]. However, quantitative comparison between shear and extensional rheology of DST suspensions remains delicate because of transient character and complexity of the flows in FiSER and CaBER experiments. Viscoelastic pinch-off experiments of Roché *et al.* [16] allowed finding the ratio of extensional-to-shear viscosities close to 3 (Trouton ratio for Newtonian fluids) above DST transition at small particle size-to-filament diameter ratios (weak confinements). This is consistent with particle level simulations of Seto *et al.* [17] showing similar energy dissipation in shear and extensional flows of bi-disperse suspensions at a ratio of big-to-small particle size higher than 1.4. These simulations have revealed an anisotropic particle microstructure under extension with the contact network (tested through a pair correlation function) somewhat diffused around the compression axis. In what concerns surface phenomena accompanying extensional flow experiments, brittle fracture of filaments reminiscent to glassy states has been typically observed above DST transition [14,15]. For pinch-off experiments, the authors have reported relatively strong undulation of the filament surface before break-up related to a sequence of jammed and fluid states as well as filament bending along its fluid parts after break-up [16].

Free surface phenomena of DST fluids have been mainly studied for vibrating DST layers exhibiting surface instabilities in the form of holes and fingers as well as in the context of impact resistance with a special accent on propagation of cracks—an important topic for body armor application—see the review by Brown and Jaeger [2] and the references therein. A recent work of Darbois Texier *et al.* [18] reports another type of surface instability observed in a film flow down an inclined plane. Surface waves emerging during this flow have visual resemblance with classical roll waves, but they arise without inertia due to the S-shape of the flow curve of DST fluids.

Falling viscous jets combine extensional and free surface flows and offer an alternative way to test the extensional rheology. However, only a few recent publications have considered jet flows of DST concentrated suspensions. Liard *et al.* [19] have studied a free-falling jet of a DST aqueous silica suspension. At high particle concentrations, the jet is shown

to develop a new type of instability manifested through rapid transverse oscillations (somewhat similar to filament bending in Roché *et al.* experiments [16]) accompanied by break-up events above some critical length. The instability has been fully ascribed to stress oscillations within the jet above DST transition. Following the motion of wave maxima, the authors have measured a distribution of forward and backward wave speeds and found that the waves are not advected by the falling jet, but the average wave speed is close to the one of a vibrating solid string under gravitational stretching. Wang *et al.* [20,21] have studied the primary break-up of aqueous cornstarch jets by an annular air jet and the secondary break-up of the DST drops by a transverse air jet, in the context of the spray atomization process. The authors report so-called “hardened” primary break-up, when, under strong shear imposed by a surrounding air jet, the suspension jet exhibits lateral oscillations and fractures into large fragments at inflection points. They also observed a hardened secondary drop break-up manifested through a hemispherical droplet shape atypical for this phenomenon.

However, in the existing works, direct relationship between suspension rheology and transverse jet oscillations is still lacking, while different important wave characteristics, like dispersion relation, frequency spectra, and root mean square (RMS) amplitude, have not been reported. To fill this gap, we propose in the present article, a detailed experimental analysis of the jet dynamics of aqueous suspensions of calcium carbonate (CC) particles based on spatiotemporal diagrams of the jet lateral drift and jet surface undulation as well as on two-dimensional (2D) Fourier spectra of these both quantities giving access to dispersion relations, wave speeds and RMS amplitude and RMS speed of the lateral drift of the unstable jet. Moreover, we study the effect of rigid polyamide (PA) fibers addition on the jet dynamics and show a strong damping of lateral oscillations with transition to a break-up regime similar to that observed for jets of Newtonian concentrated hard-sphere suspensions [22]. Finally, evaluation of the stress profile along the jet provides, if not complete understanding, a physical insight into the origin of jet instability without fibers and the effect of fiber addition on jet oscillation-to-break-up transition. As in the previously studied case of shear flow [13], the fiber orientation distribution is expected to play an important role on the rheology of CC-PA mixtures in extensional flows within the falling jets when the flow-induced fiber alignment could considerably enhance the extensional viscosity [23] and somehow influence the DST transition and, thus, the jet instability—this effect will be discussed in the present article. From the application point of view, the jet instability described in this article can, in principle, occur in different jet-based technologies, such as cement jet grouting, shear thickening polishing, abrasive jet cutting, mortar spraying, cement pumping, etc. Understanding and mastering the (in)stability of shear thickening jets are, therefore, of high practical relevance.

## II. MATERIALS AND METHODS

### A. Suspension components and preparation

The suspension is a concentrated mixture of calcium carbonate (CC) microparticles (calcite BL200 supplied by

Omya, Switzerland) at volume fraction of  $\varphi_p = 68\%$  vol dispersed in a dilute aqueous polymer solution, with addition of different concentrations of polyamide (PA) microfibers. CC particles have by far a rhomboidal shape, approximately equal in size in all directions and in this sense considered to have an isotropic shape with a characteristic size  $D_p = 5.5 \pm 2.0 \mu\text{m}$ . The particle density and specific surface area are  $\rho_p = 2525 \text{ kg/m}^3$  and  $S_p = 0.88 \text{ m}^2/\text{g}$ , respectively.

PA fibers were supplied by Pinfloc textile additives company (France), ideally scaled to our need; they were directly used without any extra-treatment. The density and the Young modulus of PA fibers are, respectively,  $\rho_f = 1140 \text{ kg/m}^3$  and  $E = 4.56 \text{ GPa}$ . The fiber average length, diameter, and aspect ratio are  $L_f = 800 \mu\text{m}$ ,  $D_f = 17 \mu\text{m}$ , and  $r = L_f/D_f \approx 47$ , respectively. The ratio of characteristic bending stress  $\sigma_{buck}$  corresponding to buckling instability to characteristic shear or tensile stresses  $\sigma$  in our experiments was evaluated as follows [24,25]:

$$\frac{\sigma_{buck}}{\sigma} \approx 1.2 \frac{E \ln(2r)}{r^4 \sigma} \quad (1)$$

and was found always to be much larger than unity for the experimental stress range. This allows considering the fibers as rigid.

A comb polymer composed of a polymethacrylate backbone with polyethylene oxide side chains denoted by PCP-45 from Chryso company (France) was used as a superplasticizer. The polymer chemical structure is presented in Ref. [10]. The weight average and number average molar masses are, respectively, 52.7 and 21.0 kg/mol.

The preparation of the suspension undergoes several steps, which can be summarized as follows. First, the mass of the CC particles is defined according to the desired CC volume fraction  $\varphi_p$  and the desired volume  $V_m$  of CC suspension:  $m_p = \rho_p V_m \varphi_p$ . The particle volume fraction is set to  $\varphi_p = 0.68$  (68% vol) of whole CC suspension. At this concentration, the DST threshold is surely to be reached, at least in the shear flow [10]. Then, the particles are mixed with an appropriate amount of the solution of PCP-45 polymer in de-ionized water of 18.2 M $\Omega$  cm resistivity. The mixture was realized using a vortex mixer by two steps of 5 min duration separated by 5 min sonication in an ultrasound bath. The polymer concentration is set to 0.002 g of dry polymer per gram of CC dry particles. Upon mixing, the PCP-45 polymer is adsorbed to the surface of the CC particles ensuring their lubrication and decrease in the suspension low-shear viscosity. This polymer concentration was chosen according to the previous work [26] and corresponds to the beginning of the adsorption isotherm plateau. During the preparation, two important rules were carefully respected. First, addition of all the components was quick and realized in a closed volume of the precision balance in order to maximally avoid water evaporation, which can dramatically change the particle concentration and shift the DST threshold to lower stresses. The second rule is to carefully stir the suspension at relatively low intensity of the vortex mixer, avoiding DST and, thus, suspension jamming during mixing.

After preparation of CC suspension at  $\varphi_p = 68\%$  vol, different amounts of PA fibers were added to the mixture, and then the suspension was mixed for another 10 min with 5 min sonication between two mixing steps. The suspension was then kept at rest for 3 h at 4 °C to achieve thermodynamic equilibrium of its components. Typical volume of the prepared CC-PA mixture was 35 ml. From fluid mechanics point of view, the final CC-PA mixture can be considered as a suspension of PA fibers dispersed at a volume fraction  $\varphi_f$ , ranging between 0% and 2% vol, in a shear thickening matrix of volume  $V_m$ . This matrix is nothing but CC suspension at a fixed CC volume fraction  $\varphi_p = 68\%$  vol defined as the ratio of CC particles' volume to the CC suspension volume  $V_m$ . The volume fraction of fibers in the CC-PA mixture is defined as the ratio of the volume  $V_f$  of PA fibers to the volume of the whole CC-PA mixture  $V$ :  $\varphi_f = V_f/V = V_f/(V_f + V_m)$ .

## B. Shear rheometry

Controlled-stress shear rheometry of CC suspensions and CC-PA mixtures was realized in our previous work mostly using the mixer type double helix tool allowing avoiding different artifacts related to particle sedimentation and suspension expulsion and providing an acceptable scale separation between fibers and rheometer gap sizes [13]. Briefly, a linearly increasing stress ramp was applied from  $\sigma = 0 \text{ Pa}$  to  $\sigma = 100 \text{ Pa}$  with a rate of stress increase of 0.33 Pa/s and the measured shear rate  $\dot{\gamma}$  was recorded with a sample rate of 2 points/s. The shear flow curves relevant for the present article are presented in Fig. 1 by dashed lines. All the flow curves exhibit an S-shape with a very sharp DST transition (assigned to the horizontal “negative” jump of the shear rate at some critical shear stress  $\sigma_c$ ) and irregular oscillations

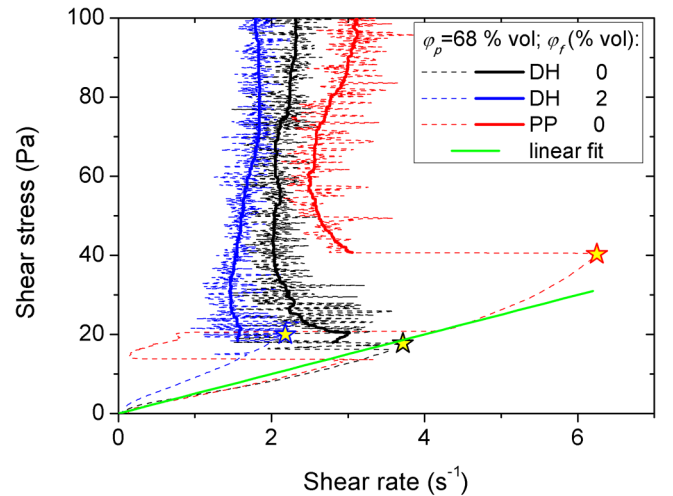


**FIG. 1.** Controlled-stress shear rheometry of CC suspensions and CC-PA mixtures conducted in two different geometries, double helix (DH) and plate-plate (PP), at a fixed CC volume fraction  $\varphi_p = 68\%$  vol and two different PA volume fractions  $\varphi_f = 0$  and 2% vol. Dashed lines correspond to “raw” flow curves containing fluctuation parts above DST transition; thick solid lines correspond to smoothed fluctuation parts; straight thin solid (green) line is a linear fit of the low-shear quasi-Newtonian part of the right (red) flow curve (PP tool,  $\varphi_f = 0$ ); star symbols indicate the break points of flow curves at which the critical DST shear rate  $\dot{\gamma}_c$  and shear stress  $\sigma_c$  are defined.

above  $\sigma_c$ . The fluctuation part of flow curves was smoothed using a 91-point median smoothing algorithm and the corresponding solid lines are superimposed on original flow curves. Such smoothing provides an estimate of time-averaged flow curves. The critical shear rate  $\dot{\gamma}_c$  of DST transition is defined at a break point of flow curves at which the shear rate exhibits its abrupt decrease. These points are labeled by star symbols for each flow curve in Fig. 1.

With increasing volume fraction of PA fibers from  $\varphi_f = 0$  to  $\varphi_f = 2\%$  vol, the flow curve shifts to the left, the critical shear rate  $\dot{\gamma}_c$  decreases, and the critical shear stress  $\sigma_c$  slightly increases. This tendency holds for intermediate volume fractions,  $\dot{\gamma}_c$  and  $\sigma_c$  values being reported in Table I, for different tested CC-PA mixtures. Such a shift has been interpreted in terms of local shear rate and shear stress arising in the pores of the PA fiber network filled with shear thickening CC suspension [13]. In fact, the local shear rate is higher than the global one acting at the scale of the whole CC-PA mixture and applied at the rheometer walls. On the contrary, the local shear stress is lower than the global one. Thus, to achieve the DST in the CC matrix at the given local shear rate and stress, one should apply a lower global shear rate and a higher global shear stress to the CC-PA mixture. A detailed analysis of the fiber volume fraction effect on critical  $\dot{\gamma}_c$  and  $\sigma_c$  values is provided in [13]. For example, a slight linear increase in  $\sigma_c$  with  $\varphi_f$  is observed for a larger fiber concentration range. However, this scaling is different from that for pure CC suspensions, for which  $\sigma_c$  decreases with  $\varphi_p$  [10,13]. This is because the physics behind  $\sigma_c(\varphi_f)$  and  $\sigma_c(\varphi_p)$  dependencies is completely different. In fact,  $\sigma_c$  in CC suspension corresponds to the critical stress of the polymer brush collapse on the CC particle surface, while  $\sigma_c$  in CC-PA mixtures is just critical stress in pure CC suspension rescaled by a factor taking into account local shear rates and depending on  $\varphi_f$ . If there is no DST in a CC suspension (at sufficiently low  $\varphi_p$ ), the DST will not appear by adding the fibers.

Notice that changing the rheometer tool from the double helix (DH) to the plate-plate (PP) tool brings some peculiarities. On the one hand, the initial (low-shear quasi-Newtonian) parts of the flow curves are similar for both tools. A linear fit of the low-shear part of the right (red) flow curve (PP tool,  $\varphi_f = 0$ ) is represented by a straight (green) solid line in Fig. 1, whose slope corresponds to the low-shear viscosity,  $\eta_0 \approx 5$  Pa s of the CC suspension without fibers. The low-shear values  $\eta_0$  for different CC-PA mixtures are reported in Table I. On the other hand, the

critical  $\dot{\gamma}_c$  and  $\sigma_c$  values are substantially higher for the PP tool [right (red) curve in Fig. 1] as compared to the DH tool [middle (black) curve]. This difference has been reported in the previous work [13] without being fully understood. It likely arises from the difference of flow fields that may influence the particle contact network and/or particle migration within the suspension. One can also remark a sudden jump of the right (red) flow curve (measured with the PP tool) below DST. It probably comes from a particle aggregate temporarily blocking the flow. This aggregate should have been destroyed by increasing shear stress because no jumps were detected at second and subsequent stress ramps, as reported in [13].

It is also worth noticing that the rheology of the CC-PA mixture could be influenced by a few other factors, such as superplasticizer concentration, interactions between CC particles and PA fibers, or fiber entanglement. However, these effects likely play a secondary role in our experimental system. First, the superplasticizer concentration (0.002 g/g CC particles—see Sec. II A, corresponding to 0.17% vol) is sufficiently low and does not change significantly the suspending liquid viscosity. Second, possible adsorption of the superplasticizer on PA fibers is expected to not affect the CC-PA mixture rheology because PA fibers are well dispersed in water with and without superplasticizer, and they have much smaller total surface as compared to CC particles (thus not changing the polymer grafting density on the CC surface). Third, CC particles do not show significant adhesion to PA fibers. Also, the excluded volume interaction and confinement effects (due to finite size ratio of CC and PA particles) have been ruled out in our previous work [13]. This seems to minimize the effect of CC/PA interactions on CC-PA mixture rheology. Finally, the possible effect of fiber entanglement can be discarded for both shear and jet flows, as long as the fiber rigidity criterion,  $\sigma_{buck}/\sigma \gg 1$  [Eq. (1)], is fulfilled for both flows.

### C. Jet flow experiments

The experimental setup of the jet flow experiment is presented in Fig. 2 and composed by a filling tank, a vertical tube of an internal diameter  $D_0 = 2R_0 = 5$  mm and length  $h = 215$  mm, connected coaxially to the bottom of the tank, a collecting Petri dish, and a fast camera Miro C110 (Phantom, US) equipped with a charge-coupled device (CCD) sensor. About 30 ml of the suspension was first poured in the tank (average diameter  $D_1 \approx 50$  mm, suspension height

**TABLE I.** Shear rheological properties of CC-PA mixtures at different fiber volume fractions.

Fiber volume fraction $\varphi_f$ (% vol)	Average <sup>a</sup> low-shear viscosity <sup>b</sup> $\eta_0$ (Pa s)	DST critical shear rate <sup>b</sup> $\dot{\gamma}_c$ (s <sup>-1</sup> )	DST critical shear stress <sup>b</sup> $\sigma_c$ (Pa)
0	5.0 ± 0.4 (5.0 ± 0.7)	3.6 ± 0.1 (6.3 ± 0.2)	16 ± 2 (40 ± 3)
0.5	5.2 ± 0.4	3.1 ± 0.1	16 ± 2
1	6.0 ± 0.5	2.6 ± 0.1	16 ± 2
2	8.5 ± 0.8	2.2 ± 0.1	20 ± 2

<sup>a</sup>Average viscosity below DST transition.

<sup>b</sup>Evaluated using the DH rheometric tool. The measurement in PP geometry was only confident for the sample at  $\varphi_f = 0$ , with the measured values given in brackets. At  $\varphi_f > 0$ , all the rheometric geometries other than DH generated several artefacts (sample expulsion, sedimentation, etc.).

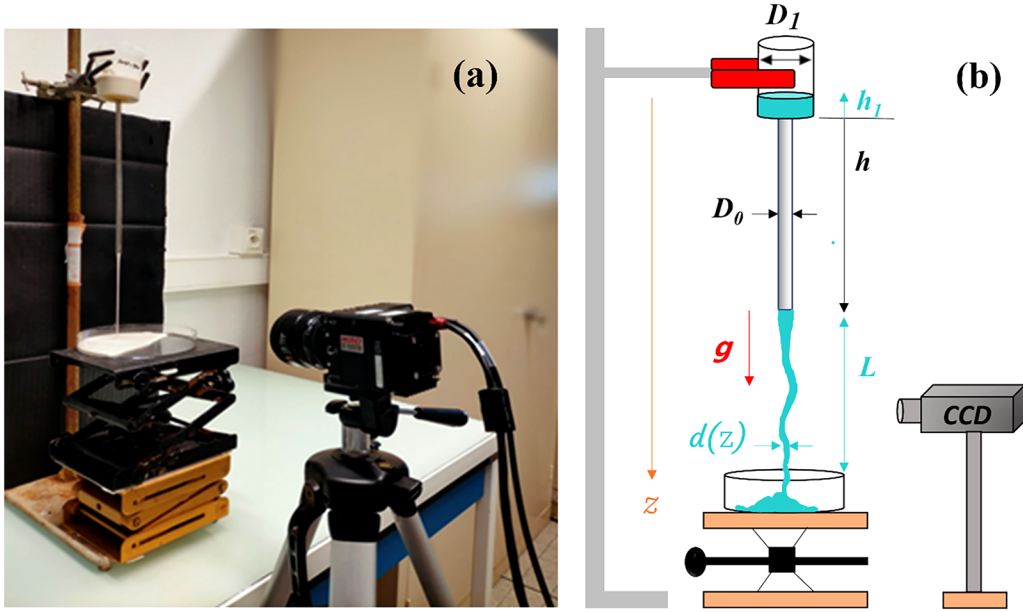


**FIG. 2.** Fast camera device for recording jets of CC-PA mixtures extending from the tube outlet to the experimental table (a). Geometric notations are introduced in (b).

$h_1 \approx 15$  mm). During the filling, the lower tube extremity was maintained open allowing the suspension to fill the tube under gravity. Then, the lower extremity was mechanically closed, and the suspension was left at rest inside the tank and the tube for 1 min. At the moment of time  $t = 0$ , the lower extremity was again opened, the suspension started flowing through the tube under gravity at nearly constant flow rate during the whole duration of the experiment (thanks to  $D_0 \ll D_1$  and  $h_1 \ll h$ ). The flow through the tube is laminar and the wall shear stress  $\sigma_w \approx \rho g R_0 / 2 \approx 25$  Pa (with  $\rho \approx 2000$  kg/m<sup>3</sup> being the suspension density and  $g \approx 10$  m/s<sup>2</sup>—gravity acceleration) is believed to be below the DST transition ( $\sim 40$  Pa) revealed in a plate-plate (PP) shear rheometry [cf. right (red) flow curve in Fig. 1]. Below DST, the CC suspension experiences nearly Newtonian behavior with the average low-shear viscosity  $\eta_0 \approx 5$  Pa s, corresponding to the linear fit of the initial part of the right (red) flow curve in Fig. 1. The velocity profile inside the tube is expected to be nearly parabolic and the mean velocity averaged over the tube cross-section is given by

$$u_0 \approx \frac{\rho g R_0^2}{32 \eta_0}. \quad (2)$$

The measured flow rate  $Q$  through the tube fits within 13% error to the theoretical value  $Q = u_0 \pi R_0^2$ . This correlates with the supposed laminar flow regime below DST transition. The stress field in the jet is supposed to be mostly extensional (at least at axial distances a few tube diameters downstream the tube outlet) with the stress levels governed by gravitational forces. All experiments were performed at room temperature of 20 °C, controlled by an air conditioner.

The dynamics of the CC-suspension jet was recorded with a high-speed camera at 336.5 fps (frames per second) and at a spatial resolution of 2.6 pixel/mm. This allowed us to

follow the falling suspension and enabled capturing the jet diameter  $d(t, z)$  (supposing preservation of the jet’s axial symmetry) and the deviation  $x(t, z)$  of the jet centerline from rectilinear trajectory (hereinafter called lateral drift) at the spatial resolution of 0.39 mm and the temporal resolution of 3.0 ms. To quantify the magnitudes  $d(t, z)$  and  $x(t, z)$ , we developed an image processing script in MATLAB (MathWorks®). Defining the background intensity with a graphical user interface, the script analyzed each frame of the movie. For each frame (each moment of time  $t$ ), the script detects the jet using a gaussian fit of the intensity profile to extract its diameter  $d(z)$  and its lateral drift  $x(z)$  along the vertical axis. In case of the jet break-up, the script also quantifies the properties of each jet segment. The script analyses each frame in a parallel workflow to optimize the computation time (230 ms/frame on a 6-core processor).

Apart from the direct analysis of the jet lateral drift  $x(t, z)$ , we performed a Two-Dimensional Discrete Fourier Transform (2D DFT) of the measured  $x(t, z)$  dependencies. To this purpose, we applied the “fft2” built-in function of the MATLAB software to the  $m \times n$  matrix of  $x$  values, whose  $m = 5000$  rows and  $n = 364$  columns correspond to discrete values of  $t$  and  $z$ , respectively. The “fft2” function returns a  $m \times n$  matrix  $\mathbf{A}$  of complex values, using the following expression:

$$A_{p+1, q+1} = \sum_{j=0}^{m-1} \sum_{l=0}^{n-1} \exp\left(-\frac{2\pi i}{m} j p - \frac{2\pi i}{n} l q\right) x_{j+1, l+1}, \quad (3)$$

where  $i = \sqrt{-1}$  stands for the imaginary unit,  $p = 0, 1 \dots m - 1$ , and  $q = 0, 1 \dots n - 1$ . For better presentation, we shifted the zero-frequency component of the matrix  $\mathbf{A}$  to the center of the spectrum using “fftshift” built-in MATLAB function. This function swaps the first quadrant of  $\mathbf{A}$  with the

third, and the second quadrant with the fourth. The components of the matrix  $\mathbf{X}$  of the Fourier spectrum amplitudes were then calculated as  $X_{j,l} = |A_{j,l}|/(m \cdot n)$ , with the rows  $j = 1, \dots, m$  and columns  $l = 1, \dots, n$  corresponding to discrete values  $\omega_j = 2\pi f_t(j - m/2)/m$  and  $k_l = 2\pi f_z(l - n/2)/n$  of the temporal angular frequency  $\omega$  and wave numbers  $k$ , respectively. Here,  $f_t = 336.5 \text{ s}^{-1}$  (fps) is temporal sampling rate fixed by the camera speed and  $f_z = 2.6 \text{ mm}^{-1}$  (pixel/mm) is the spatial sampling rate fixed by image resolution. In this way, we obtained a discrete  $X(\omega, k)$  dependency of the Fourier amplitude on temporal and spatial frequencies. The final signal  $X(\omega, k)$  allowed evaluation of dominant frequency and wavelength of jet lateral oscillations as well as the dispersion relation, which was retrieved as a curve  $\omega(k)$  drawn along the crests of  $X(\omega, k)$  surface plots. A similar 2D DFT analysis was applied to the jet diameter  $d(t, z)$  with the Fourier spectrum amplitude denoted by  $\mathfrak{D}(\omega, k)$ .

Notice that the “instrumental” sampling rates  $f_t = 336.5 \text{ s}^{-1}$  and  $f_z = 2.6 \text{ mm}^{-1}$  appeared to be too large as compared to maximal observable frequencies in  $X(\omega, k)$  and  $\mathfrak{D}(\omega, k)$ -transforms. Thus, prior to Fourier transform, we had to “coarse” the recorded data [by removing appropriate lines and columns of the  $x(t, z)$  and  $d(t, z)$ -matrices and reducing the  $m \times n$  matrix size] to achieve the sampling rates just slightly larger than twice the maximal observable frequency. In this way, the Nyquist limit was still respected.

For quantitative comparison of the intensity of lateral oscillations, we also evaluate a root mean square (RMS) amplitude  $x_{RMS}$  of the lateral drift and RMS transverse speed  $v_{RMS}$  of the jet. These parameters are directly defined from the Fourier amplitudes using the Plancherel theorem, as follows:

$$x_{RMS} = \sqrt{\sum_{j=1}^m \sum_{l=1}^n X_{j,l}^2}, \quad (4)$$

$$v_{RMS} = \sqrt{\sum_{j=1}^m \sum_{l=1}^n (X_{j,l}^2 \omega_j^2)}, \quad (5)$$

with the summation performed over all elements of the Fourier amplitude matrix  $\mathbf{X}$ .

### III. RESULTS AND DISCUSSION

#### A. Qualitative observations

In this subsection, we report the visualization experiments conducted on the jet of CC-suspension or CC-PA mixtures. First, we consider the CC mixtures without PA fibers and evaluate the effect of the jet length on the jet dynamics [Sec. III A 1]. Second, we consider CC-PA mixtures and evaluate the effect of PA fiber addition on the behavior of the jet [Sec. III A 2].

##### 1. Effect of the jet length

In this subsection, we inspect the jets of CC suspension without addition of PA fibers. At a given flow rate, depending on the jet length, different behaviors are observed, as shown on snapshots of Fig. 3. At the jet length  $L \lesssim 4 \text{ cm}$ , the jet

remains strictly vertical and cannot be distinguished from a Newtonian viscous thread [Fig. 3(a)]. Viscoelastic coiling instability (typically reported for honey-like fluids [1]) then takes place at  $4 \text{ cm} \lesssim L \lesssim 6 \text{ cm}$ , when the jet extremity describes circular motion on the experimental table, while the whole jet exhibits precession motion around the tube axis [Fig. 3(b)]. These two first regimes have been extensively studied in literature and are out of scope of the present article. Increasing the suspension jet length above  $L \gtrsim 6 \text{ cm}$  suddenly gives place to another form of instability. The falling jet no longer follows a straight vertical trajectory but undergoes lateral drifts (oscillations) with well-distinguishable running waves in both downstream and upstream directions [Fig. 3(c)]. At  $L \gtrsim 15 \text{ cm}$  and at axial positions  $z \gtrsim 15 \text{ cm}$ , we notice periodic rupturing of the jet into solid-like segments, which after falling on the experimental table keep their cylindrical shape for a few seconds before melting to become liquid again. As it was reported, the DST state for a shear thickening fluid keeps for a few seconds after applied shear stress removal [27]—duration long enough for the jet to stay in the DST state after it breaks and until it hits the experimental table. These observations on lateral oscillations and solidification effects agree with the previous work of Liard *et al.* [19] on the jets of silica particle suspensions.

#### 2. Effect of the PA volume fraction

Addition of PA fibers to CC suspension qualitatively changes the jet behavior, and these changes depend on the PA volume fraction. In Fig. 4, the jet of CC-suspension without PA fibers is compared with jets of CC-suspension with three different concentrations of PA fibers. The jet length is fixed to 15 cm. The jet of CC-suspension without PA fibers [Fig. 4(a)] is continuous and laterally oscillating all along its length. The generation of these oscillations may be due to stress fluctuations in the jet above a critical stress of DST transition, as typically observed in confined CC-suspension in shear-rheological measurements [2]. Addition of PA fibers globally decreases the lateral oscillations [Figs. 4(b)–4(d)] and stops them completely (i.e., the jet becomes completely vertical) in the concentration interval  $0.7\% \text{ vol} < \varphi_f < 0.8\% \text{ vol}$ . This effect will be explained and quantitatively evaluated in Sec. III C 2. However, with increasing fiber concentration, the break-up events become more frequent and occur at shorter distances  $L_b$  from the tube outlet, called hereinafter the break-up length. It is possible that with increasing PA volume fraction, PA fibers form larger flocs inside the jet, whose size likely becomes comparable to the jet diameter leading to the jet break-up, as it occurs with the jet of concentrated suspension of spheres [22]. This point will be inspected in Sec. III C 3 along with quantitative evaluation of the break-up length. For the better understanding of CC-PA jet behaviors, the movies corresponding to the four snapshots of Fig. 4 are presented in Ref. [28].

#### B. Quantitative analysis of jet dynamics

We analyze in this subsection, the dynamics of the jets of CC-PA mixtures through different quantitative features, such as the jet diameter, lateral drift, Fourier spectra, dispersion relation, and wave speed.



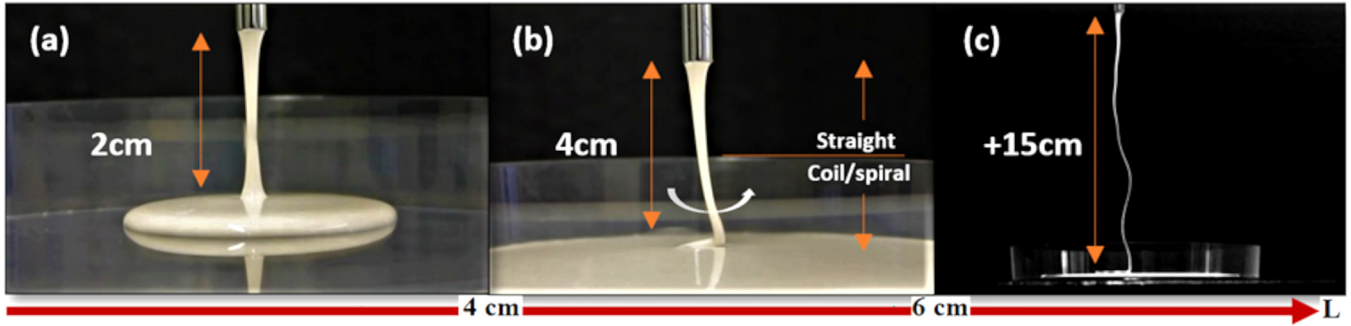


**FIG. 3.** Snapshots of the falling CC-suspension jet without PA fibers: stable viscous jet (a); jet subject to coiling instability (b); and jet subject to lateral oscillations (c). The average length-to-diameter ratio is  $L/D_0 \approx 4.0$ ,  $8.0$ , and  $30$  for jets shown in (a), (b), and (c), respectively.

### 1. Variation of the jet diameter

The suspension jet shows some fluctuations of its diameter along its length and during time. For quantitative analysis of these fluctuations, we evaluated first the mean jet diameter,  $\langle d \rangle = f(z)$  averaged over time as a function of the axial position, as plotted in Fig. 5(a) for the CC-PA mixtures at  $\varphi_f = 0, 0.6, 1.2$ , and  $2\%$  vol, with  $\varphi_f = 0$  corresponding to CC suspension without fibers. The average jet diameter was evaluated excluding zero values of the instantaneous jet diameter during possible jet ruptures. For all the curves, we observe an initial rather strong decrease in the diameter in the downstream direction attributed to gravitational stretching, as typically observed for free falling jets [1]. This decrease is followed by a slight increase in the average diameter at the bottom part of the jet due to jet flow deceleration near the point where the jet hits the experimental table. We also notice that the average jet diameter is a growing function of the fiber volume fraction. This is expected from higher viscosity of CC-PA mixtures with higher  $\varphi_f$  values; the jet of a more viscous fluid exhibits less thinning diameter when stretched by gravity. For example, in the viscous regime at short axial distances, the Newtonian jet radius scales as  $R \sim u^{-1/2} \sim \eta_0(\rho g)^{-1/2} z^{-1}$  (with  $u$  being the jet speed at a given axial position  $z$ )—see, for instance, Ref. [29]. To quantify jet break-up events that happen at some conditions, we introduce the break-up probability  $\Pi$  at a given axial position  $z$  as a ratio

of time  $T_{d=0}$  interval, for which zero instantaneous jet diameter was detected, to the observation time interval  $T$ , namely,  $\Pi = (T_{d=0}/T) \times 100(\%)$ . Experimental  $\Pi(z)$ -dependency is plotted in Fig. 5(b) for various  $\varphi_f$  values. As inferred from this figure, the break-up probability is zero all along the jet of CC suspension without fibers, in agreement with observations of the jets with length  $L < 15$  cm, cf. Sec. III A 1. The break-up probability increases dramatically with fiber volume fraction and achieves  $80\%$  at the jet lower section at  $\varphi_f = 2\%$  vol. The axial probability profile has a sigmodal shape at  $\varphi_f = 1.6$  and  $2\%$  vol, with zero break-up probability until some critical break-up length  $L_b$ , followed by a gradual increase at  $z > L_b$ . The effect of the PA fiber volume fraction on the break-up length will be inspected in Sec. III C 3 in conjunction with theoretical estimations.

Then, we evaluated the deviation  $\Delta d(t, z) = d(t, z) - \langle d \rangle(z)$  of the instantaneous jet diameter  $d(t, z)$  from its average value; the spatiotemporal maps (colormaps) of the  $\Delta d(t, z)$  function are plotted in Figs. 6(a), 6(c), 6(e), and 6(g) for the observation time lapse of 5 s and for the same range of the fiber volume fraction  $\varphi_f$  as in Fig. 5. The colormaps at  $\varphi_f = 0$  and  $0.6\%$  vol clearly show a periodic sequence of the yellow (thicker diameter) and blue (thinner diameter) bands corresponding to the blobs and necks along the jet length. In a grayscale image, the yellow and blue bands are perceived as clearer and darker bands, respectively. The amplitude of

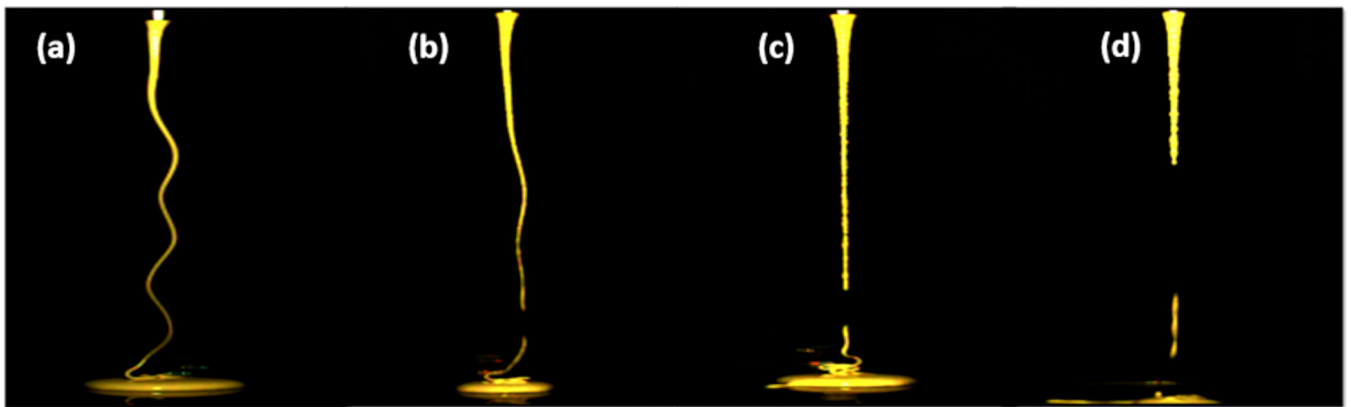


**FIG. 4.** Snapshots of suspension jets at different PA fiber concentrations (Ref. [28]). (a) CC suspension without PA fibers. The jet is completely unstable showing a wavy pattern along its length. (b) CC-PA mixture at  $\varphi_f = 0.6\%$  vol. The jet is still unstable and presents some ruptures in the bottom section. (c) CC-PA mixture at  $\varphi_f = 1.6\%$  vol. The jet is stable against lateral oscillations with frequent ruptures occurring at the bottom section of the jet. (d) CC-PA mixture at  $\varphi_f = 2\%$  vol. The jet is completely stable against lateral oscillations with frequent ruptures all along the jet length.

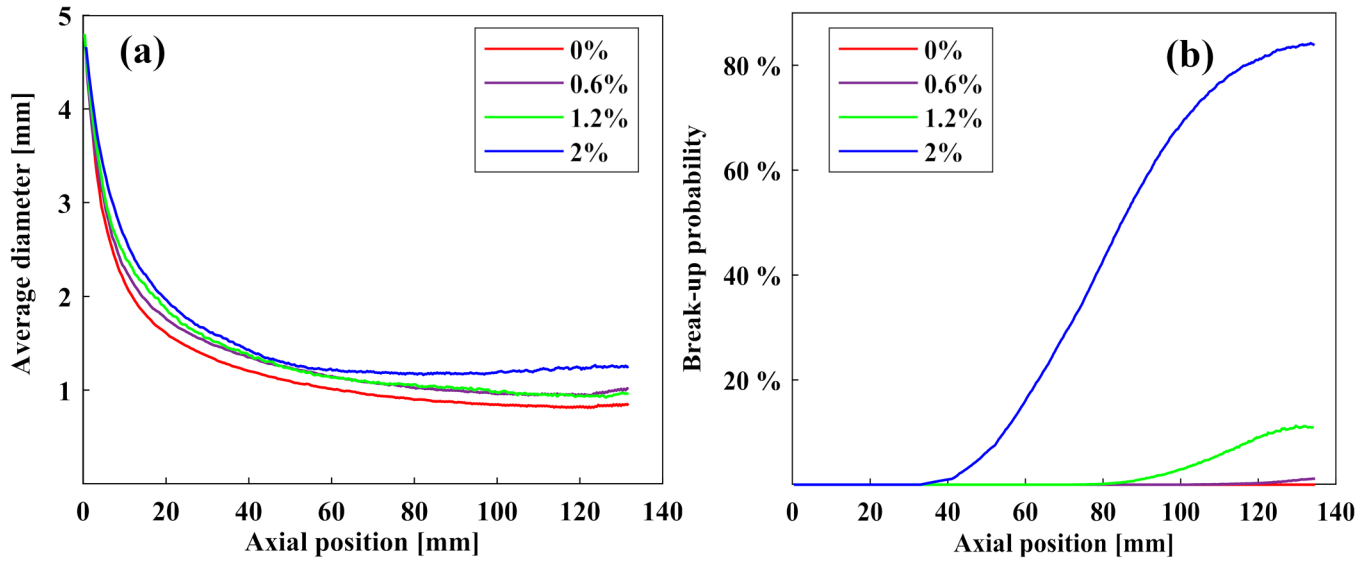


FIG. 5. Jet diameter  $\langle d \rangle$  averaged over observation time (a) and the jet break-up probability (b) as a function of the axial position  $z$  for CC-PA mixtures at different PA volume fractions listed in the figure legend.

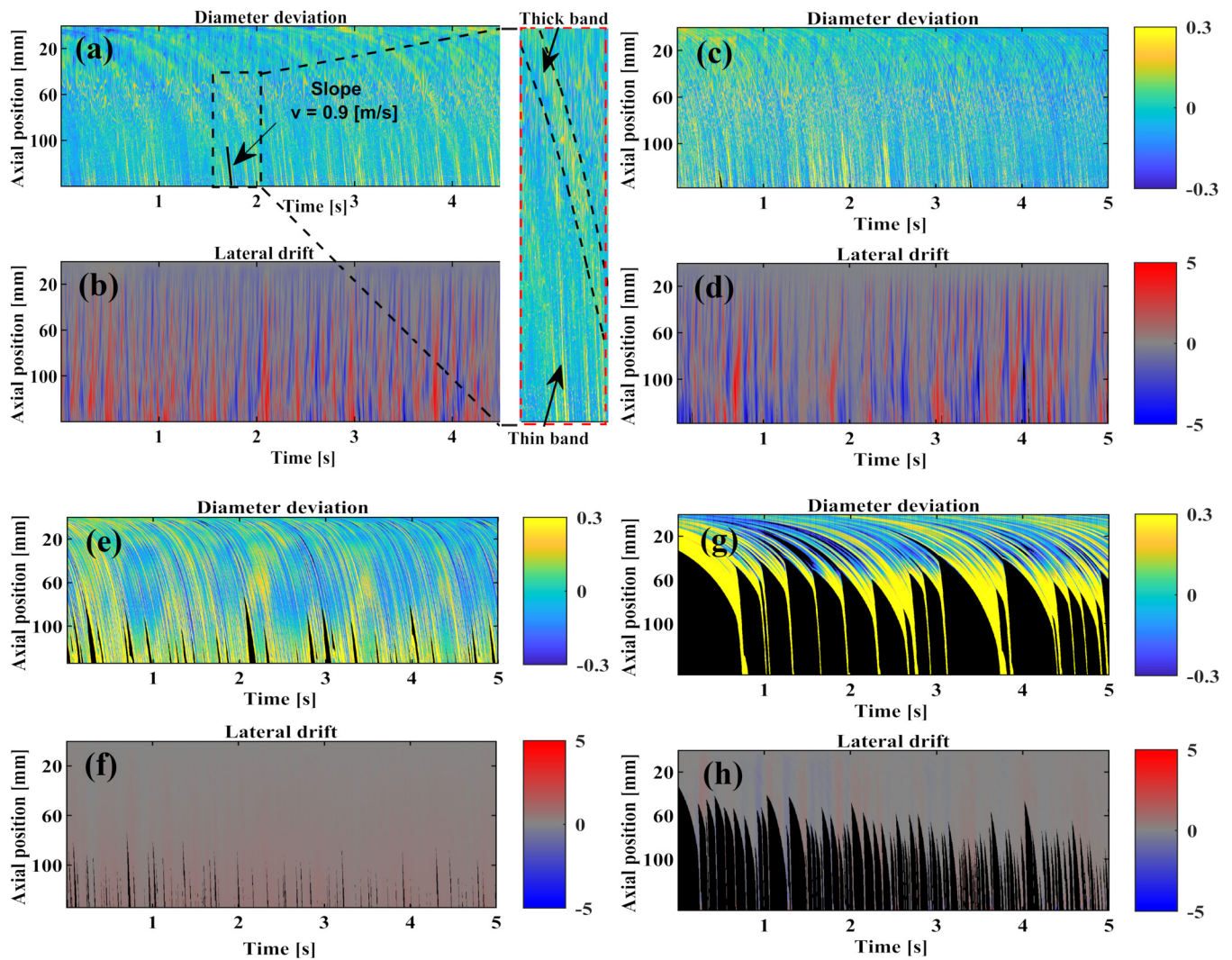


FIG. 6. Spatiotemporal diagrams of the jet diameter deviation  $\Delta d(t, z)$  [in mm, parts (a), (c), (e), and (g)] and jet lateral drift  $x(t, z)$  [in mm, parts (b), (d), (f), and (h)] for CC-PA mixtures at different PA fiber volume fractions:  $\varphi_f = 0$  (CC suspension in the absence of fibers) (a) and (b); 0.6% vol (c) and (d), 1.2% vol (e) and (f), and 2% vol (g) and (h). The inset on the right of (a) and (b) shows an enlarged view of a rectangular region of the  $\Delta d(t, z)$ -map (a) delimited by the dashed line. Thin yellow (clear) bands and thick bands delimited by inclined dashed curves are distinguished on this inset.

these surface undulations is relatively small ( $\pm 0.3$  mm) with respect to wavelengths  $\sim 10 - 150$  mm and the jet mean diameter of 1–5 mm. Such surface undulations have not been detected in jet instability experiments of Liard *et al.* [19] likely because of space resolution limits, as opposed to relatively strong undulation of the filament surface in pinch-off experiments of Roché *et al.* [16]. A negative slope of the color bands in the  $(t, z)$ -space [Fig. 6] points out to the downstream propagation of the blobs-and-necks sequence along the jet flow direction. An enlarged view of the colormap in Fig. 6(a) is provided in the inset of Fig. 6 and reveals complex dynamics of surface undulations with two kinds of blobs. On the one hand, thick bands clearly visible in non-zoomed views correspond to relatively long blobs travelling along the jet with a relatively low speed gradually increasing in the downward direction. On the other hand, in the lower half of the jet, we detect a sequence of thin yellow (clearer) and blue (darker) bands, corresponding to shorter and faster blobs and necks, each travelling at a high constant speed of about 0.9 m/s, as inferred from the slope of the thin yellow bands—one of these slopes being shown in Fig. 6(a). The speed of two kinds of blobs appears to be much higher than the jet speed, which increases from  $\sim 8 \times 10^{-4}$  to  $\sim 0.02$  m/s along the jet. In addition to it, one can easily observe the jet ruptures designated by black colored sections. The ruptures are absent at  $\varphi_f = 0$ ; some rare break-up events appear at the jet lower section for  $\varphi_f = 0.6\%$  vol; the ruptures become frequent and appear closer to the tube outlet for  $\varphi_f = 1.2$  and 2% vol, in agreement with observations in Sec. III A 2 and with the break-up probability plotted in Fig. 5(b).

For a deeper analysis of blob-and-neck propagation, we perform a 2D DFT analysis of the jet diameter  $d(t, z)$ , as specified in Sec. II C. The contour plots of the amplitude  $\mathfrak{D}(\omega, k)$  of the Fourier spectrum in the frequency domain  $(\omega, k)$  are presented in Fig. 7 for CC-PA mixtures at different fiber volume fractions. At  $\varphi_f = 0$  and 0.2% vol, we observe an elongated pattern extended from the second to the fourth quadrant [Figs. 7(a) and 7(b)], which looks like a mountain crest in a surface 3D plot (not shown here for brevity). This crest corresponds to surface undulation waves propagating downstream the flow. In general, the projection of the crest onto the horizontal  $(\omega, k)$ -plane is described by some function  $\omega = f(k)$ , which is nothing but a wave dispersion relation. In Figs. 7(a) and 7(b), the crests have a linear shape [denoted by a dashed line in Fig. 7(a)] corresponding to non-dispersive waves on the jet surface with a linear dispersion relation  $\omega = v_s k$ . The wave speed  $v_s$  is defined as an average slope of experimental  $\omega = f(k)$  dependencies.

Interestingly, for  $\varphi_f \geq 0.5\%$  vol, we observe two separate amplitude crests [highlighted by dashed lines in Fig. 7(c)], still having a linear shape associated to two different wave speeds for the same propagation direction. This situation is expected to reflect a more complex dispersion relation that may physically correspond to wave propagation through heterogeneous and/or anisotropic media, which may admit different wave speeds, as often reported for elastic waves in granular media [30], porous media [31], or fibrous materials [32]. In our case, the addition of PA fibers likely brings some anisotropy (in case of nonrandom orientation distribution of

fibers along the jet flow) and/or large-scale heterogeneity [in the case of formation of flocs perceived at the rough jet surface—see Figs. 4(c) and 4(d)]; this probably results in two wave speeds. Further investigations are required to clarify this point. Notice, however, that two crests visible in Figs. 7(c) and 7(d) should not be confounded with the “slow” and “fast” blobs detected in the spatiotemporal maps in Figs. 6(a) and 6(c) because the “slow” blobs propagated with a speed varying along the jet, while the wave speeds assigned to the wave crests in Figs. 7(c) and 7(d) are constant and, therefore, more relevant for “fast” blobs. The “slow” blobs dynamics is likely masked by relatively broad central spot of the Fourier spectra in Fig. 7. In addition to it, we do not have a clear explanation for the thin horizontal bands appearing at  $\omega \approx \pm 370$  rad/s $^{-1}$  in all contour plots of Fig. 7. It is not expected to come from acoustic wave resonance of the suspension-filled tube (with fundamental frequency of  $\sim 2 \times 10^4$  s $^{-1}$ ) but is probably caused by the resonance with the mechanical support of the fluid tank [Fig. 2].

In what concerns the wavelength range, for all fiber volume fractions, the Fourier amplitude is significant at relatively small wavenumbers and decays above  $k_{max} \approx 500$  m $^{-1}$ . This corresponds to surface undulation wavelengths ranging between  $\lambda_{min} = 2\pi/k_{max} \sim 10$  mm and the observable jet length  $\lambda_{max} \sim L \approx 150$  mm. Let us now evaluate two characteristic wavelengths of the Rayleigh-Plateau (RP) instability, which are the critical wavelength of the instability onset [1],  $\lambda_c = 2\pi R_0 \approx 15$  mm and the most amplified wavelength [1],  $\lambda_m = 2\pi R_0 [2 + 3\eta_0(\rho\gamma R_0/2)^{-1/2}]^{1/2}$ , which is equal to 96–124 mm for our CC-PA samples, where  $\gamma \approx 0.072$  N/m is the surface tension. As we see, both RP wavelengths enter the interval of the surface undulation wavelengths observed in our experiments. However, as we will see in Sec. III B 2, the wave speed in our case is much larger than that of the RP instability, which is equal to the jet speed.

As it will be seen in Sec. III B 2, the blob-and-neck propagation along the jet at  $\varphi_f < 0.8\%$  vol is accompanied by lateral oscillations of the jet centerline. So, the fluctuations of the jet diameter and jet centerline seem to be governed by the same physics related to DST transition in the extensional flow along the jet, as will be inspected in Sec. III C.

## 2. Lateral oscillations

The spatiotemporal maps of the jet lateral drift are presented in Figs. 6(b), 6(d), 6(f), and 6(h). It is well observed that the jet of CC-suspension without PA fibers is continuous and represents no ruptures [Fig. 6(b)], as has been shown in the same figure in diameter deviation colormaps [Fig. 6(a)] and agrees with zero break-up probability shown by the red (the lowest) line in Fig. 5(b). The sequence of blue and red bands (perceived, respectively, as darker and clearer bands in a grayscale image) in the lateral drift colormaps corresponds to negative (to the left from the tube axis) and positive (to the right from the tube axis) drift of the jet during time, thus indicating that the jet is strongly oscillating. The color bands appear to be nearly vertical meaning that mostly the whole jet displaces to the left or to the right with respect to the tube axis. We also note that the color intensity varies (and

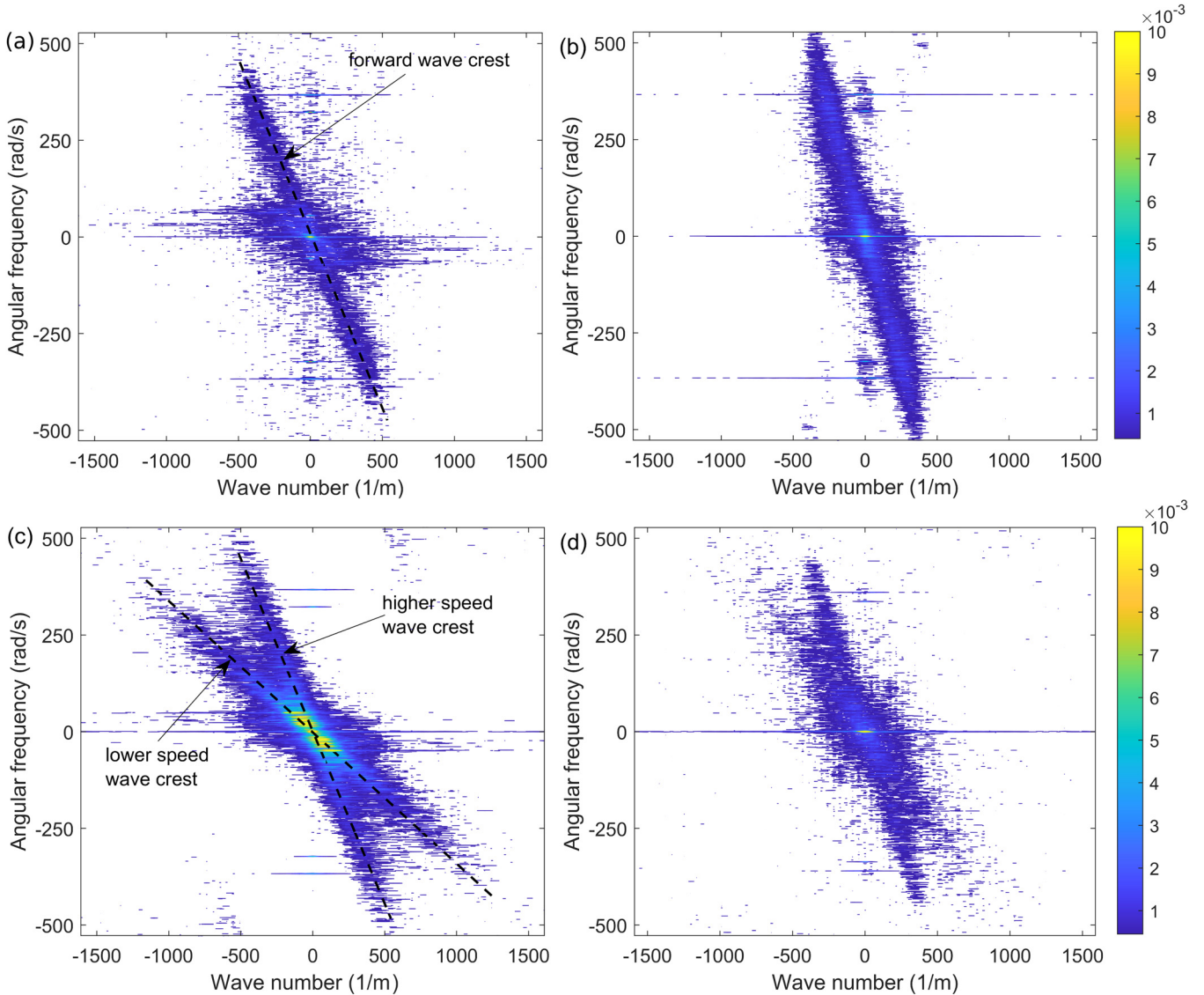


**FIG. 7.** Contour plots of the Fourier amplitude  $\mathfrak{D}(\omega, k)$  (in mm) of the jet instantaneous diameter  $d(t, z)$  of the CC-PA mixtures at different PA volume fractions:  $\varphi_f = 0\%$  vol (a), 0.2% vol (b), 0.5% vol (c), and 0.7% vol (d). The dashed lines in (a) and (c) are guides for eye to follow either a single wave speed (a) or two different wave speeds (c). The color bars of (a) and (c) are similar to those of (b) and (d). The sampling rates were fixed to the values  $\omega_{up} \approx 1060$  rad/s and  $k_{up} \approx 3200$  m $^{-1}$  slightly larger than twice the highest observable  $\omega$  and  $k$  values (cf. Sec. II C). The lowest nonzero  $\omega$  and  $k$  values are fixed by the film duration (14.86 s) and the observed jet length ( $\sim 145$  mm) that gives  $\omega_{down} \approx 0.423$  rad/s and  $k_{down} \approx 43.3$  m $^{-1}$ .

sometimes fluctuates) vertically along the bands becoming more intense in the downstream direction. This means that, as expected, the lateral drift is more pronounced at higher axial positions, while color intensity fluctuations reflect jet centerline undulations along the jet, as observed in experimental snapshots [Figs. 4(a) and 4(b)] and movies [28].

The jet is not totally continuous and the ruptures along its length sometimes occur when adding PA fibers at 0.6% vol [Fig. 6(d)], but the rupture events are still seldom at this PA volume fraction, in agreement with weak (a few %) values of the break-up probability—see the purple (the second from the bottom) line in Fig. 5(b). In the lateral drift colormaps, the rare rupture events appear as a few relatively thin black bands or spots. The ruptures become more pronounced when increasing the PA fiber concentration, as inferred from the increasing number of black bands in colormaps for  $\varphi_f = 1.2\%$  vol [Fig. 6(f)] and 2% vol [Fig. 6(h)]. This correlates with the

increasing break-up probability revealed from Fig. 5(b). However, the jet becomes completely stable at fiber volume fraction  $\varphi_f \geq 0.8\%$  vol and lateral oscillations disappear. For example, the lateral drift colormaps for  $\varphi_f = 1.2\%$  vol [Fig. 6(f)] and 2% vol [Fig. 6(h)] are rather homogeneous (with nearly zero lateral drift), except for the black bands at the lower part of the jet standing for the jet ruptures.

For a finer analysis of the jet lateral drift  $x(t, z)$ , the 2D DFT analysis was performed on the  $x(t, z)$  signal, as detailed in Sec. II C. The obtained surface plot of the Fourier spectrum  $X(\omega, k)$  at  $\varphi_f = 0$  is shown in Fig. 8(a), and the contour plots  $X(\omega, k)$  for different PA fiber volume fractions are shown in Figs. 8(c)–8(f). We observe two main crests in the surface plot of Fig. 8(a), one spanning the odd quadrants and corresponding to the forward propagation of the jet lateral drift, and another one spanning the even quadrants and assigned to the backward wave propagation. A secondary crest at the middle plane of the

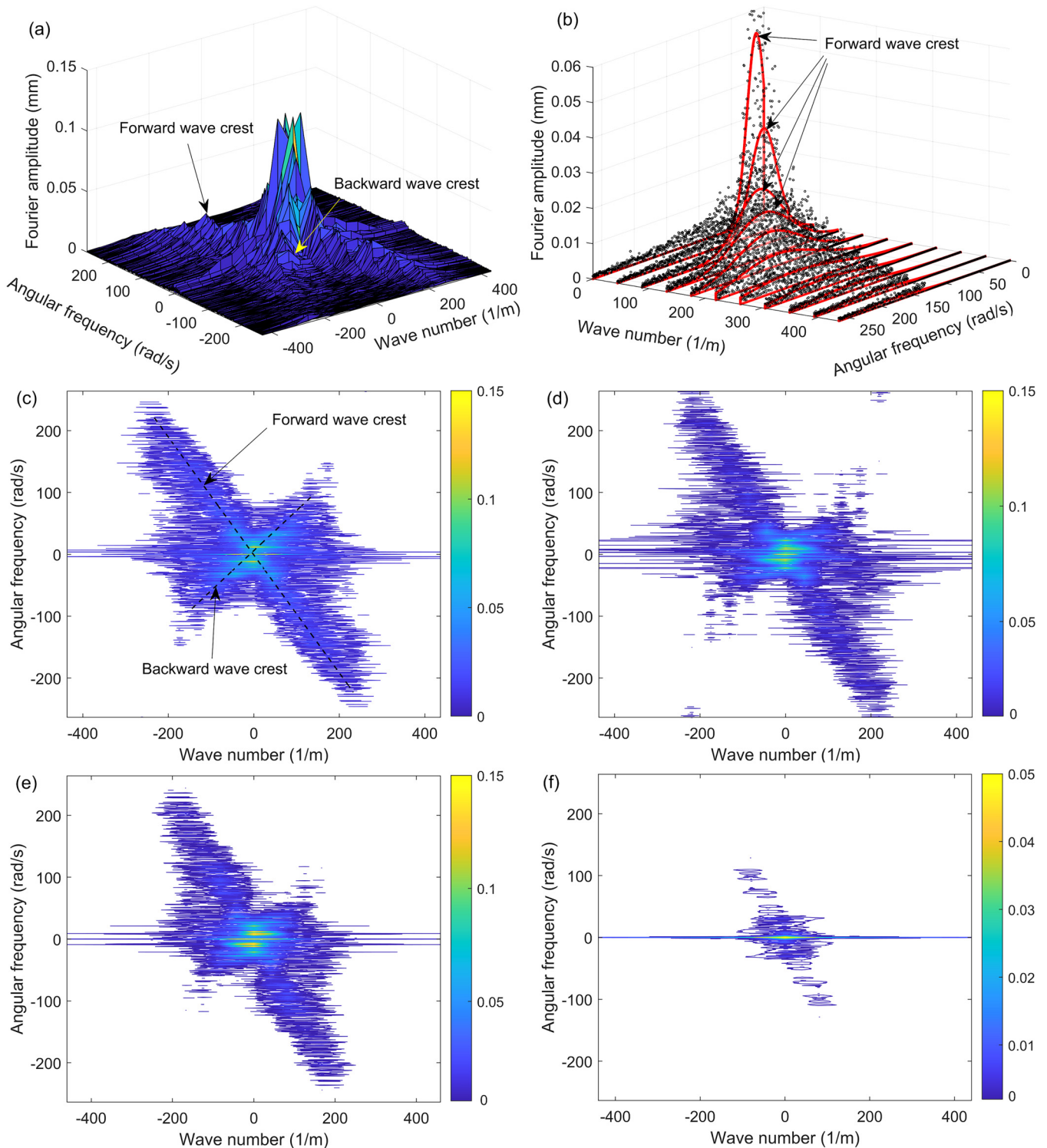


**FIG. 8.** Fourier amplitude  $X(\omega, k)$  (in mm) of the jet lateral drift  $x(z, t)$  of the CC-PA mixtures at different PA volume fractions: surface plot (a), 3D scatter plot of the second quadrant ( $\omega \leq 0, k \geq 0$ ) after sign inversion of  $\omega$  (b) and contour plot (c) for  $\varphi_f = 0$  (CC suspension without PA fibers); contour plots for  $\varphi_f = 0.6\%$  vol (d),  $0.7\%$  vol (e), and  $0.8\%$  vol (f). The red lines in (b) (having a bell-like shape) correspond to the gaussian fit of each vertical slice (along the lines  $k = \cos nt$ ) of the 3D scatter plot. The black dashed lines in (c) are guides for eye helping one to follow the forward and backward wave crests. The sampling rates were fixed to values  $\omega_{up} \approx 530$  rad/s and  $k_{up} \approx 860$  m $^{-1}$  slightly larger than twice the highest observable  $\omega$  and  $k$  values (cf. Sec. II C). The lowest nonzero  $\omega$  and  $k$  values are fixed by the film duration (14.86 s) and the observed jet length ( $\sim 145$  mm) that gives  $\omega_{down} \approx 0.423$  rad/s and  $k_{down} \approx 43.3$  m $^{-1}$ .

surface plot (perceived in the contour plots as a horizontal band centered at  $\omega = 0$ ) likely corresponds to some slow dynamics occurring at the jet speed  $u \approx 8 \times 10^{-4} - 0.02$  m/s. The contour plots in Figs. 8(c)–8(f) allow one to appreciate the “width” of the crests, their extension through the  $(\omega, k)$

domain, and the difference between forward and backward wave crests. The shape and the height of the crests deserve a detailed analysis.

The projection of crests [Fig. 8(a)] onto a horizontal  $(\omega, k)$  plane gives a dispersion relation  $\omega = f(k)$  corresponding to

the wave propagation of lateral oscillations. The dashed lines in Fig. 8(c) indicate an approximate position of both main wave crests. Strictly speaking, the dispersion relation can be exactly established for infinitely thin (and infinitely high) crests with the Fourier amplitude along the crests respecting the Dirac delta function—a hypothetical case of zero damping (e.g., inviscid fluid) and the infinitely long jet. In our case of highly viscous suspension, the crests are much more diffuse, so we have defined the dispersion relation in the following way. First, we isolated a single quadrant of the Fourier spectrum corresponding to either the forward or the backward wave. Second, the residual amplitudes corresponding to the secondary (low frequency) crest were manually eliminated, and the rest of the  $X(\omega, k)$  data lower than some threshold were set to zero (filtered) in order to reduce the noise. Third, the 3D scatter plot of the pretreated  $X(\omega, k)$ -signal was generated [Fig. 8(b)] and sliced by vertical planes parallel to the  $\omega$ -axis and corresponding to fixed discrete values of wavenumber  $k$ . Each slice contained a point cloud  $X_k(\omega)$  that was fitted by a gaussian function shown by red solid lines (having a bell-like shape) in Fig. 8(b). The location of peaks of each gaussian curve was assigned to the crest position in the  $(\omega, k)$ -plane that allows a clear definition of the dispersion relation. Remarkably, the discrete points of the dispersion relation always gathered along a straight line and, therefore, were fitted by a linear function  $\omega = v_l k$ . Such a linear dispersion relation (found for forward and backward waves at all fiber volume fractions) corresponds to nondispersive waves and the slope  $v_l$  stands for the wave speed. Notice that for the present case of nondispersive waves, the phase speed  $\omega/k = v_l$  is the same as the group speed  $d\omega/dk = v_l$ .

From the theoretical perspective, Liard *et al.* [19] has supposed that wave propagation along the shear thickening jet is equivalent to vibration of a solid taut string with gravity playing the role of the tensile force. Following this idea, the wave speed squared is given by  $v_l^2 = \tau/\rho$ , where  $\tau$  is the tensile force by unit jet cross-section. In the ideal string

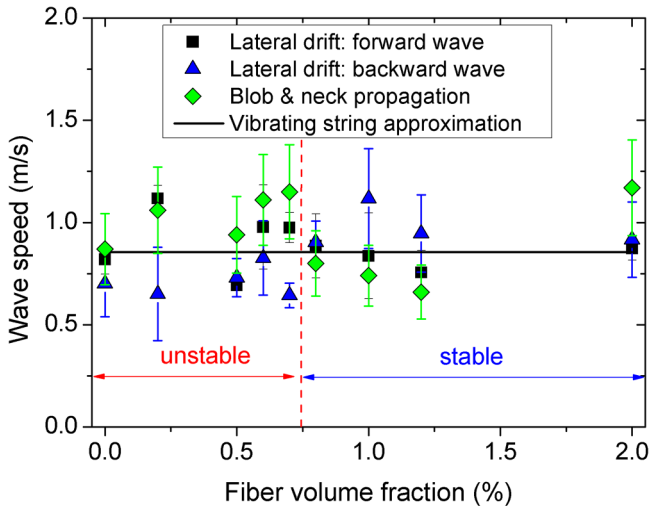


FIG. 9. Effect of the fiber volume fraction on forward/backward wave speeds  $v_l$  of the jet lateral oscillation and on blob-and-neck propagation speed  $v_s$ . Here, we use the highest of two  $v_s$  values for comparison with  $v_l$ .

model, the tensile force is constant along the string, while in our case of gravitational stretching, it varies linearly with the axial position:  $\tau = \rho g z$ , resulting in  $v_l^2(z) = g z$ . It can be shown that the last expression is valid in a short-wave limit  $\lambda \ll L$  and under assumptions of nearly constant jet cross section and high wave speeds  $v_l \gg u$ . Notice that our Fourier analysis provides some effective wave speed likely related to the RMS value of  $v_l(z)$ , which, in the frames of the vibrating string model, is given by

$$v_l = \sqrt{\frac{1}{L} \int_0^L v_l^2(z) dz} = \sqrt{\frac{gL}{2}}, \quad (6)$$

recalling that  $L \approx 0.15$  m is the total jet length.

Experimental and theoretical [Eq. (6)] dependencies of the wave speed on the fiber volume fraction are shown in Fig. 9 for forward (black squares) and backward (blue triangles) waves. The error bars correspond to the confidence interval of the linear fit of gaussian peak locations [cf. Fig. 8(b)]. Experimental values show some fluctuation with the fiber volume fraction without deserving any clear tendency. One can observe near similar (within experimental errors) speeds of forward and backward waves. This suggests the single dispersion relation for both propagation directions. Noteworthy, the wave speed  $v_s$  of blob-and-neck propagation (green diamonds) is the same (within the error bars) as the wave speed  $v_l$  of lateral oscillations. For the CC-PA samples with two blob-and-neck wave speeds [Figs. 7(c) and 7(d)], we use the highest of two  $v_s$  values for comparison with  $v_l$ . Quantitatively, we find the average value of these speeds  $v_l \approx v_s \approx 0.9 \pm 0.2$  m/s independent of the fiber volume fraction. This value is in excellent agreement with the speed propagation of the “fast” blobs,  $\sim 0.9$  m/s, directly revealed from the spatiotemporal maps in Fig. 6. The similarity between  $v_l$  and  $v_s$ -values could point out to the same origin of both instabilities coming from fluctuating stresses above DST transition. On the other hand, the jet surface undulations are typically observed for RP instability, occurring due to capillary forces. However, the speed of the surface undulation propagation is about the jet speed for RP instability. In our experiments, the jet speed varies from  $\sim 8 \times 10^{-4}$  m/s at the tube outlet to  $\sim 0.02$  m/s at the jet lower extremity and remains much lower than wave speed  $v_s \sim 1$  m/s. This could be an argument for ruling out the RP instability in our case.

The “vibrating string” model does not distinguish between the jets with and without fibers and provides a single wave speed  $v_l \approx 0.87$  m/s independently of the fiber volume fraction (horizontal black line in Fig. 9), provided that the jet is in the “solid” state above the DST critical stress. Despite data dispersion, our experiments seem to confirm this tendency and show a very good quantitative agreement with the model ( $0.9 \pm 0.2$  m/s in experiments vs 0.87 m/s in theory). Ignoring the tensile force variation along the jet, Liard *et al.* [19] have obtained the expression  $v_l = \sqrt{gL}$  for wave speed, which differs from our one [Eq. (6)] by a factor of  $\sqrt{2} \approx 1.4$ . In their experiments, they used a completely different DST fluid (concentrated suspension of silica particles) at a different jet length  $L \approx 0.08$  m as compared to our experimental

value  $L \approx 0.15$  m. They have found similar average values of forward and backward wave speeds, both about half of their theoretical value. They attribute this difference to the phase lag between forward and upward waves. However, their experimental value  $v_l \approx 0.45$  m/s is relatively close (within large statistical errors) to the prediction of Eq. (6) that gives  $v_l \approx 0.63$  m/s. More data have to be collected for establishing exact scaling of the wave speed as a function of the jet length. At this stage, we can constate that the vibrating string model [Eq. (6)] provides a good wave speed prediction for two different experimental systems.

Surprisingly, the wave speeds  $v_l$  and  $v_s$  are also similar for unstable (at  $\varphi_f < 0.8\%$  vol) and stable (at  $\varphi_f \geq 0.8\%$  vol) jets. This correlates with the vibrating string model: both kind of jets exhibit the same wave speeds independently of the origin of their vibration, whether it comes from self-excitation in unstable jets or external random vibrations (sound, small mechanical shocks) of stable jets. The difference is in the oscillation amplitude, which is of course significantly lower (if not vanishing) for stable jets, as it will be shown below.

It is instructive to inspect now the intensity of different harmonics of the jet lateral drift. The most relevant magnitude for this purpose is the Fourier amplitude measured along the crests of the Fourier spectra, hereinafter called “crest height.” We defined it experimentally as height  $X_c(k)$  of the gaussian peaks associated to each discrete value of the wavenumber  $k$  [red bell-shaped curves in Fig. 8(b)]. The confidence interval of the gaussian fit was assigned to the uncertainty (error bar) of crest height determination. The magnitude  $L_c(k) = \sqrt{\omega^2(k) + (v_l k)^2} = v_l k \sqrt{2}$  is considered as a dimensionally correct measure of the “crest length,” with the wave speed  $v_l$ -values being taken from experiments [Fig. 9] for each distinct CC-PA mixture. Experimental  $X_c(L_c)$ -dependencies obtained in a parametric form [ $L_c(k), X_c(k)$ ] are shown in Figs. 10(a) and 10(b) for forward and backward waves, respectively, and for different PA fiber volume fractions. Zero frequency values  $X_c(0)$  of the crest height that correspond to a lateral offset of the jet centerline are excluded from the plots because they may change between different experimental runs and must vanish when averaged over a large number of runs.

We see that the crest height gradually decreases with the crest length. The maximal  $X_c$ -value (excluding zero frequency) corresponds to the lowest nonzero discrete wavenumber value  $k_{down} \approx 43.3 \text{ m}^{-1}$  imposed by the observable jet length. Thus, for both propagation directions, the dominant wavelength corresponds to the jet length:  $\lambda_{max} = 2\pi/k_{down} \approx L \approx 0.15$  m. On the opposite limit, the shortest distinguishable wavelength can be arbitrarily assigned to that having an amplitude about 10% of the maximal amplitude at  $k = k_{down}$ . This gives  $k_{max} \approx 280 \text{ m}^{-1}$ ,  $\lambda_{min} = 2\pi/k_{max} \approx 20$  mm for the forward waves and  $k_{max} \approx 140 \text{ m}^{-1}$ ,  $\lambda_{min} \approx 40$  mm for backward waves. This corroborates with a shorter extension of backward wave crests observed in the contour plots of Fig. 8. In general, the crest height of backward waves is lower than that of forward ones. On the other hand, we can conclude that the jet surface undulation and forward waves of jet lateral oscillations exhibit near similar wavelength range,  $\lambda = 0.01(0.02) - 0.15$  m. It can also be seen that the oscillation amplitude is high for CC-PA

mixtures at fiber volume fractions  $\varphi_f \leq 0.7\%$  vol but abruptly decreases at  $\varphi_f = 0.8\%$  vol, in agreement with direct observations showing that jet lateral oscillations disappear at  $\varphi_f \gtrsim 0.8\%$  vol [Sec. III A 2]. Thus, at higher fiber concentrations,  $\varphi_f = 1$  and  $1.2\%$  vol, the Fourier amplitudes are no longer discernable from the errors of the data processing, especially taking into account strong artifacts related to the jet break-up.

The possible reasons for jet lateral oscillations, stabilization by fibers, and for the transition from lateral oscillation regime to jet break-up with increasing fiber content will be inspected in Sec. III C in conjunction with theoretical evaluations.

### C. Theoretical insight

In this subsection, we try to give the responses on two main questions of the present work through a few theoretical evaluations employing the jet’s momentum balance. The two questions are: (a) Do the jet transverse oscillations come from the DST transition? (b) What is the effect of the fibers on the qualitative and quantitative changes of the jet dynamics?

#### 1. Stress profile along the jet of pure CC suspension

We restrict our analysis to the steady state flow inside the jet and a straight vertical shape of the jet. This is expected to suffice for the analysis of the instability onset and the effect of fiber addition on the instability threshold. In this subsection, we consider only the jets of CC suspensions without PA fibers. We follow Sauter and Buggisch [33] who derived the momentum balance equation from the force balance acting on a jet horizontal slice under inertia, capillary, gravity, and viscous forces. The flow is classically assumed to be purely extensional with the axial velocity  $u$  depending only on the axial  $z$  coordinate. The original derivation covering only Newtonian fluids is easily extended to non-Newtonian rheology and gives the following set of steady-state equations for the evolution of the velocity  $u$ , the jet radius  $R$ , and the tensile stress  $\sigma_E = \sigma_{zz} - \sigma_{rr}$  with the axial position  $z$  (here,  $\sigma_{zz}$  and  $\sigma_{rr}$  are the axial and radial normal stresses, respectively):

$$\rho u \frac{du}{dz} = \frac{1}{R^2} \frac{d}{dz} (\sigma_E R^2 + \gamma R) + \rho g, \quad (7a)$$

$$u R^2 = u_0 R_0^2, \quad (7b)$$

$$\frac{du}{dz} = \dot{\epsilon}(\sigma_E) = \frac{\sigma_E}{3\eta_0 \eta_{E,r}(\sigma_E)}, \quad (7c)$$

where  $\gamma \approx 0.072$  N/m is the suspension surface tension,  $\dot{\epsilon}(\sigma_E)$  is the extension rate at a given axial position  $z$ ,  $\eta_0$  is the low-shear viscosity of CC suspension corresponding to the quasi-Newtonian regime well below DST transition [Sec. II B, Fig. 1], and the factor 3 in Eq. (7c) corresponds to the Trouton ratio [23];  $\eta_{E,r}(\sigma_E) = \eta_E(\sigma_E)/(3\eta_0)$  is the relative extensional viscosity of the non-Newtonian CC suspension

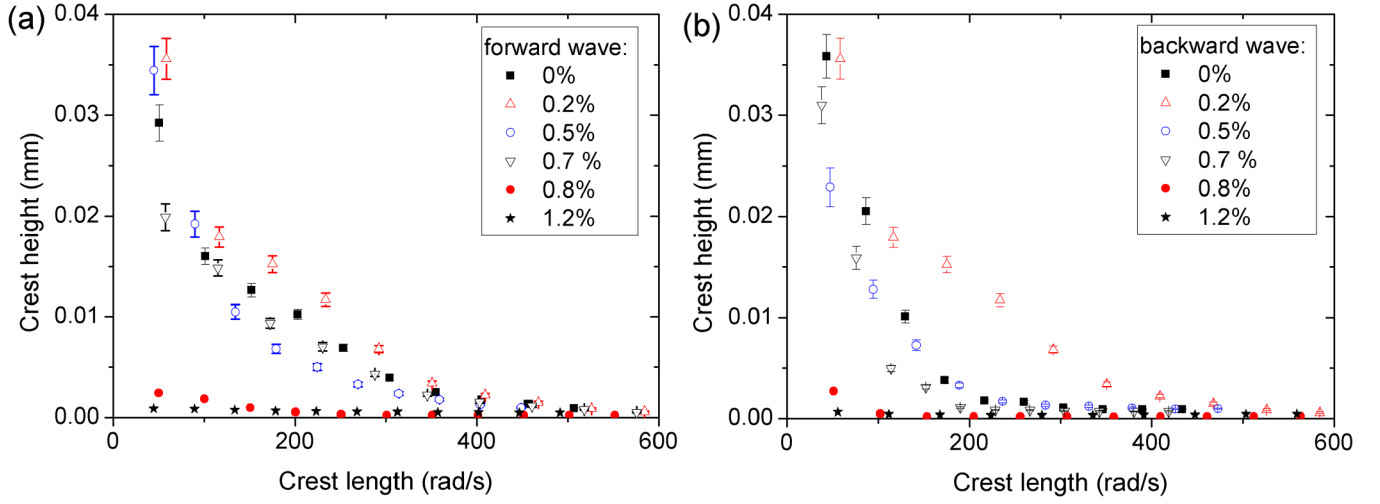


**FIG. 10.** Dependency of the crest height on the crest length for lateral oscillations at different fiber volume fractions (indicated in the legends) and for forward waves (a) or backward waves (b).

defined as a ratio of the extensional suspension viscosity  $\eta_E(\sigma_E)$  to its extensional viscosity  $3\eta_0$  at low extension rate. Equation (7b) is nothing but the flow rate conservation along the jet, with the jet speed at the tube outlet ( $z = 0$ ) given by Eq. (2), while the Eq. (7c) is the rheological relationship for the extensional flow along the jet.

Let us now introduce the following scaling factors for the velocity, the jet radius, the axial position, and the tensile stress:

$$[u] = u_0 = \frac{\rho g R_0^2}{32\eta_0}; [R] = [z] = R_0; [\sigma_E] = \rho g R_0. \quad (8)$$

The dimensionless quantities,  $\tilde{u}$ ,  $\tilde{R}$ ,  $\tilde{z}$ , and  $\tilde{\sigma}_E$ , are obtained by dividing respective dimensional quantities by appropriate scaling factors. Combining Eqs. (7a), (7b), and (7c), we arrive to the single differential equation for  $\tilde{\sigma}_E(\tilde{u})$  taking the following dimensionless form:

$$\tilde{u} \frac{d}{d\tilde{u}} \left( \frac{\tilde{\sigma}_E}{\tilde{u}} + \frac{\beta}{\sqrt{\tilde{u}}} - \varepsilon \tilde{u} \right) = -\frac{3\eta_{E,r}(\tilde{\sigma}_E)}{32\tilde{\sigma}_E}, \quad (9)$$

where  $\beta = (L_c/R_0)^2 = \gamma/(\rho g R_0^2)$ ,  $\varepsilon = u_0^2/(gR_0) = \rho^2 g R_0^3 / (1024\eta_0^2)$ , and  $L_c = \sqrt{\gamma/(\rho g)}$  is the capillary length. To get the speed dependency on the axial position, we use Eq. (7c) in the dimensionless form as follows:

$$\frac{d\tilde{u}}{d\tilde{z}} = \frac{32\tilde{\sigma}_E}{3\eta_{E,r}(\tilde{\sigma}_E)}. \quad (10)$$

It is known that the forward integration of Eq. (9) at an arbitrary initial value of  $\tilde{\sigma}_E(1)$  leads to solution divergence at large speeds  $\tilde{u}$  [29]. This problem is commonly handled by backward integration with the initial condition physically corresponding to the inertial regime at infinite speed far below the tube outlet. This corresponds to the free fall speed  $u_\infty = \sqrt{2gz_\infty}$ , the extensional rate  $\dot{\varepsilon}_\infty = \sqrt{g/(2z_\infty)} = g/u_\infty$ ,

and the tensile stress at vanishing extension rate  $\sigma_E(u_\infty) = 3\eta_0\dot{\varepsilon}_\infty = 3\eta_0 g/u_\infty$  or in the dimensionless form,

$$\tilde{\sigma}_E(\tilde{u}_\infty) = \frac{3\eta_0 g}{\rho g R_0 u_0 \tilde{u}_\infty} = \frac{3}{32\tilde{u}_\infty}. \quad (11)$$

Thus, choosing the initial point at  $\tilde{u}_\infty = 10^4 - 10^5$  and the terminal point at  $\tilde{u} = 1$  (tube outlet), we obtain numerical solution to the initial value problem [Eqs. (9) and (11)] in terms of  $\tilde{\sigma}_E(\tilde{u})$ -dependency, which, in the case of Newtonian rheology, is equivalent to common representation in coordinates  $d\tilde{u}/d\tilde{z} = f(\tilde{u})$ . The dependency of the flow speed on the axial position can further be obtained in inverse form by forward integration of Eq. (10),

$$\tilde{z}(\tilde{u}) = \frac{3}{32} \int_1^{\tilde{u}} \frac{\eta_{E,r}(\tilde{\sigma}_E(\tilde{u}))}{\tilde{\sigma}_E(\tilde{u})} d\tilde{u}. \quad (12)$$

Thus, varying the dimensionless speed in the interval  $1 \leq \tilde{u} \leq \tilde{u}_\infty$ , we get the axial position as a function of speed with the help of Eq. (12), while the  $\tilde{\sigma}_E(\tilde{z})$ -dependency is obtained in the parametric form  $[\tilde{z}(\tilde{u}); \tilde{\sigma}_E(\tilde{u})]$ .

First, we apply this calculation procedure to the Newtonian limit, which is usually appropriate for shear thickening suspension below DST transition. To this purpose, we put  $\eta_{E,r}(\tilde{\sigma}_E) = 1$  in Eqs. (9) and (12) and plot in Fig. 11(a) the  $\tilde{\sigma}_E(\tilde{u})$  theoretical dependency (solid red line) in the double logarithmic scale for typical values  $\beta = 0.66$  and  $\varepsilon = 2.44 \times 10^{-5}$  of parameters in our experiments. This dependency has a typical nonmonotonic shape of  $d\tilde{u}/d\tilde{z} = f(\tilde{u})$  dependencies reported in literature for Newtonian jets [29,33]. The initial increase in the tensile stress with speed corresponds to the viscous regime with the stress  $\tilde{\sigma}_E(\tilde{z}) \sim \tilde{z} \sim \sqrt{\tilde{u}}$  and the final decrease stands for the inertial regime with  $\tilde{\sigma}_E \sim 1/\tilde{u}$  [cf. Eq. (11)].

The basic assumption of this work is that the onset of the jet oscillation corresponds to the onset of the DST regime at some lower DST threshold stress, which should from now be distinguished from the upper DST threshold stress above



which the stress again exhibits a smooth variation with the shear or extensional rate. To check this point, we need to introduce a constitutive rheological equation for a DST fluid under the extensional flow within the jet. As it follows from particle level simulations [17], the S-shape of flow curves (typically observed under shear [Fig. 1]) is also expected under extension. At such condition, the Wyart and Cates (WC) model [5] (originally developed for shear flows) could be extended to the extensional flow. Briefly, the WC model is based on the assumption of a continuous transition between fully lubricated contacts between particles at low stresses and fully frictional contacts at high stresses with a built-up of a dense contact network. The conceptual basis of this model seems to hold in the extensional flow, as inferred from simulations of the suspension microstructure [17]. We have to bear in mind that the WC model describes only steady-state flows. It anticipates the stress range of the unstable flow but is unable to describe flow fluctuations. However, as stated above, the assumption of the steady-state condition should still be adequate for finding, at least semi-quantitatively, the onset of jet instability. Thus, extending the steady-state WC model to the extensional flow, we get the following expression for the relative extensional viscosity,  $\eta_{E,r} = \eta_E/(3\eta_0)$ :

$$\eta_{E,r}(\tilde{\sigma}_E) = \left( \frac{1 - \varphi_p/\varphi_L}{1 - \varphi_p/\varphi_J(\tilde{\sigma}_E)} \right)^2, \quad (13a)$$

$$\varphi_J(\tilde{\sigma}_E) = \varphi_F f(\tilde{\sigma}_E) + \varphi_L(1 - f(\tilde{\sigma}_E)), \quad (13b)$$

$$f(\tilde{\sigma}_E) = \exp\left(-\left(\frac{\tilde{\sigma}_{E,c}}{\tilde{\sigma}_E}\right)^\Lambda\right), \quad (13c)$$

where  $\varphi_p = 0.68$  (68% vol) is the CC particle volume fraction;  $\varphi_J(\tilde{\sigma}_E)$  is the so-called jamming volume fraction of particle suspension depending on proportion  $f(\tilde{\sigma}_E)$  of frictional versus lubricated contacts between particles;  $\varphi_F$  and  $\varphi_L$  are two limiting values of  $\varphi_J$ , corresponding to fully frictional or fully lubricated contacts;  $\tilde{\sigma}_{E,c}$  is the characteristic stress of the DST transition in extension, normalized by  $[\sigma_E] = \rho g R_0$ ; and  $\tilde{\sigma}_{E,c}$  approaches the lower DST threshold  $\tilde{\sigma}_{E,l}$  at high values of the stretching exponent  $\Lambda$ . The factor  $(1 - \varphi_p/\varphi_L)$  in the numerator of Eq. (13a) appears because the relative viscosity was not introduced with respect to the viscosity of the suspending liquid (water) of CC suspension but with respect to the Newtonian suspension viscosity  $\sim (1 - \varphi_p/\varphi_L)^{-2}$  at low extensional rates. The equation (13c) is one of the simplest empirical laws for the fraction of frictional contacts used in the literature.

For the case of the DST fluid, we conducted the backward integration of Eq. (9) replacing  $\eta_{E,r}$  by Eq. (13a). The theoretical flow curves in extension are plotted in dimensionless form in Fig. 11(b) where the dimensionless extensional rate on the abscissa axis is the function of  $\tilde{\sigma}_E$  calculated as  $\tilde{\dot{\epsilon}} = \tilde{\sigma}_E / \eta_{E,r}(\tilde{\sigma}_E)$ . All the flow curves were simulated at the CC particle volume fraction  $\varphi_p = 0.68$ , used in experiments, the packing fractions  $\varphi_F = 0.72$  and  $\varphi_L = 0.685$  used in our

previous work for the fitting of the shear flow curves (cf. supplementary material in [13]), and at two values  $\Lambda = 5$  and 50 of the stretching exponent.

The shape of simulated flow curves in extension is qualitatively similar to the shape of the shear flow curve [Fig. 1] at a relatively high value  $\Lambda = 50$  of the stretching exponent [green (lower) and blue (upper) dashed lines in Fig. 11(b)]. Furthermore, the value  $\Lambda = 50$  provides the lower DST threshold stress  $\tilde{\sigma}_{E,l}$  very close to the characteristic stress  $\tilde{\sigma}_{E,c}$  intervening into Eq. (13c). Anyway, both values of  $\Lambda = 5$  and 50 provide a linear initial section of the flow curve extending up to the DST threshold. This linear section has the same slope at both  $\Lambda$  values corresponding to the relative extensional viscosity  $\eta_{E,r}(\tilde{\sigma}_E) = 1$ , as expected for the Newtonian regime below DST transition.

For the calculation of the tensile stress profile along the jet, we have chosen two characteristic values of the characteristic stress, the first one  $\tilde{\sigma}_{E,c} = 2$  being lower than the peak value  $\tilde{\sigma}_{E,m} \approx 2.85$  of the Newtonian  $\tilde{\sigma}_E(\tilde{u})$  curve [red solid line in Fig. 11(a)] and the second one  $\tilde{\sigma}_{E,c} = 3.5$  being higher than  $\tilde{\sigma}_{E,m}$ . The value  $\tilde{\sigma}_{E,c} = 3.5 > \tilde{\sigma}_{E,m}$  at  $\Lambda = 50$  provides the tensile stress profile perfectly collapsing to the Newtonian profile [compare blue dashed and red solid lines in Fig. 11(a)]. This is expected because at  $\tilde{\sigma}_{E,c} = 3.5$ , the tensile stress does not achieve the lower DST threshold all along the jet and suspension rheology remains perfectly Newtonian, as inferred from Fig. 11(b). On the other hand, the value  $\tilde{\sigma}_{E,c} = 2 < \tilde{\sigma}_{E,m}$  at  $\Lambda = 50$  provides a strong change in the tensile stress profile [green dashed line in Fig. 11(a) perceived as clear upper dashed line in a grayscale image]. Recalling that the profile is obtained by the backward integration, the  $\tilde{\sigma}_E(\tilde{u})$  curve follows the Newtonian profile (red solid line) when the speed decreases from its terminal value  $\tilde{u}_\infty = 10^4$  up to some critical value  $\tilde{u}_c$  and the tensile stress increases from  $\tilde{\sigma}_E(\tilde{u}_\infty) = 3/(32\varepsilon\tilde{u}_\infty)$  [Eq. (11)] up to a value of the lower DST threshold  $\tilde{\sigma}_{E,l} \approx \tilde{\sigma}_{E,c} = 2$ . At lower speeds,  $\tilde{u} < \tilde{u}_c$ , the tensile stress experiences a sharp (but mathematically continuous) increase until reaching a peak value  $\tilde{\sigma}_{E,m} \approx 50$  being an order of magnitude higher than the peak value  $\tilde{\sigma}_{E,m} \approx 2.85$  of the Newtonian profile. It is quite intuitive to suppose that the surface of the tensile stress jump cannot sustain steady-state and likely moves along the jet with some speed. This surface is likely subject to corrugation instability by analogy with propagation of the shock wave front, when initially flat horizontal front develops growing wavy patterns [34]. This could lead to asymmetric shear stresses that are expected to bend initially the straight jet. However, at this moment, we have not managed to formulate the linear stability analysis proving this hypothesis. Notice that decreasing the value of the stretching exponent to  $\Lambda = 5$  allows a slightly broader region of the tensile stress profile above DST transition [black dashed line in Fig. 11(a) perceived as a dark dashed line in a grayscale image] with the stress jump always occurring at the lower DST threshold  $\tilde{\sigma}_{E,l} \approx 1.6$  which is somewhat lower to the imposed value  $\tilde{\sigma}_{E,c} = 2$  of the characteristic DST stress in the WC model [cf. black dashed (intermediate) curve in Fig. 11(b)]. In summary, whatever  $\Lambda$  and  $\tilde{\sigma}_{E,c}$  values chosen in simulations, the tensile stress jump and, presumably, the jet instability

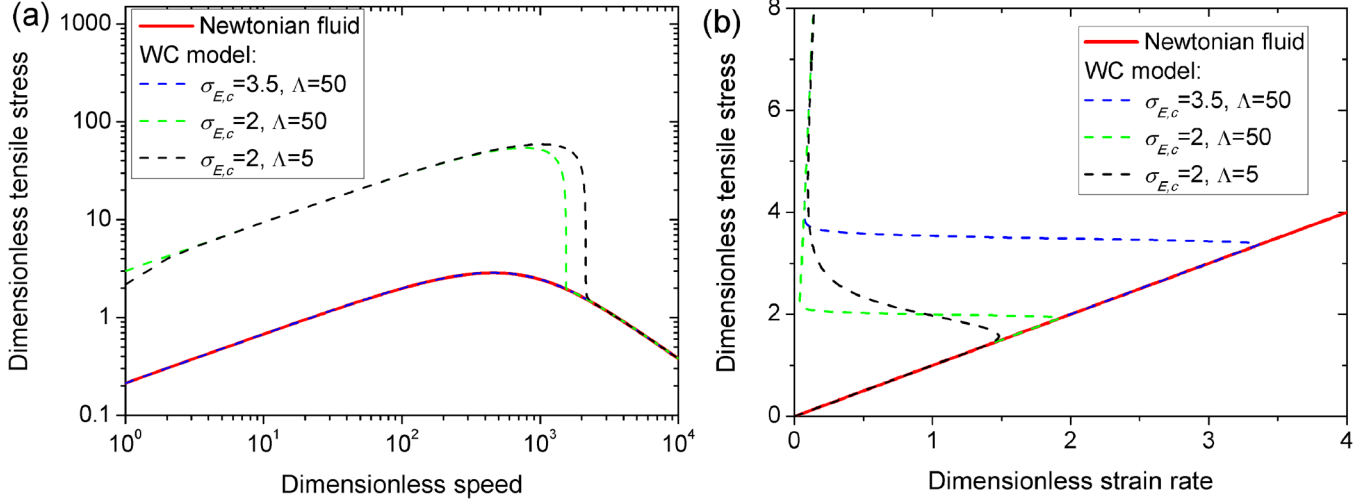


**FIG. 11.** Theoretical stress profile (in log-log scale) along the jet of the CC particle suspension in terms of the dimensionless tensile stress as a function of dimensionless jet speed (a). Theoretical flow curves for extensional rheology of CC particle suspension (b). Both plots (a) and (b) are made for the Newtonian jet (red solid line) and for the DST WC rheological model (dashed lines) with different values of  $\tilde{\sigma}_{E,c}$  and  $\Lambda$  parameters.

occur only if the lower DST threshold stress  $\tilde{\sigma}_{E,l}$  is lower than the peak value  $\tilde{\sigma}_{E,m} \approx 2.85$  of the Newtonian stress profile. In terms of dimensional magnitudes, this gives the DST tensile stress  $\sigma_{E,l} \lesssim 143$  Pa comparable to the DST shear stress  $\sigma_c \approx 20\text{--}50$  Pa measured in plate-plate or mixer type shear rheometry [Fig. 1]; see also Ref. [13].

Notice finally that the slender jet approximation used in the present study along with the backward integration scheme is not valid for the initial part of the jet,  $z \lesssim R_0$ , and leads to incorrect values of the tensile stress at the tube outlet ( $z = 0$ ) for both Newtonian and shear thickening jets [cf. nonzero  $\tilde{\sigma}_E$  values at the ordinate axis in Fig. 11(a)]. However, this artifact has a minor influence on the shape of the stress profile at  $z \gtrsim R_0$ .

## 2. Effect of fibers on jet stability

Let us now inspect the effect of fiber addition to the tensile stress profile along the jet. From now, we will restrict our analysis to the Newtonian case below DST in order to compare dimensional values of the lower threshold stress  $\sigma_{E,l}$  and the peak tensile stress  $\sigma_{E,m}$  of the Newtonian stress profile. The addition of fibers impacts the relative extensional viscosity  $\eta_{E,r}$  in Eqs. (9) and (12) and the parameter  $\varepsilon$  in which the low-shear viscosity  $\eta_0$  of the shear thickening matrix (CC suspension) should be replaced by the shear viscosity  $\eta = \eta_0 \eta_r$  of the CC-PA mixture:  $\varepsilon = \rho^2 g R_0^3 / (1024 (\eta_0 \eta_r)^2)$  with  $\eta_r = \eta / \eta_0$  being the relative shear viscosity of PA fiber suspension with respect to the low-shear viscosity of the shear thickening matrix. In the Newtonian regime below DST, both relative viscosities  $\eta_{E,r}$  and  $\eta_r$  are stress-independent but depend on the volume fraction  $\varphi_f$  of fibers and on their orientation. As in experiments we do not have access to fiber orientation, we will consider two limiting cases of isotropic orientation and fully aligned orientation when all the fibers are parallel to the extension axis (jet axis  $z$  in Fig. 2). The values of  $\eta_{E,r}$  and  $\eta_r$  are obtained using the rheological Phan-Thien and Graham (PTG)

model [35] developed for a wide concentration range of fiber suspensions and slightly modified in our previous work [13],

$$\eta_r = \frac{\eta}{\eta_0} = 1 + 2\varphi_f + G\psi_S, \quad (14a)$$

$$\eta_{E,r} = \frac{\eta_E}{3\eta_0} = 1 + 2\varphi_f + \frac{1}{3}G\psi_E, \quad (14b)$$

$$G = \frac{\varphi_f(2 - \varphi_f/\varphi_m) r^2 f^{\parallel}(r)}{3(1 - \varphi_f/\varphi_m)^2 \ln(2r)}; \quad (14c)$$

$$f^{\parallel}(r) = \frac{1 + 0.64/\ln(2r)}{1 - 1.5/\ln(2r)} + \frac{1.659}{\ln^2(2r)},$$

where  $\psi_S = a_{1212}$  and  $\psi_E = a_{1111}$  are the shear and extensional components of the fourth rank fiber orientation tensor  $\mathbf{a}$  (the subscripts 1 and 2 stand for the velocity and the velocity gradient directions, respectively), whose values are summarized in Table II for two chosen fiber orientations;  $\varphi_m = 5.4/r$  is the maximum packing fraction of fiber suspension taken at the upper limit of the granular suspension of rods [36]. Notice that the relative shear and extensional viscosities take the same value for isotropic fiber orientation.

The stress profile in terms of dimensional  $\sigma_E(z)$ -dependency is plotted in Fig. 12 for CC suspension without PA fibers (red/lower line) and CC-PA mixture at  $\varphi_f = 1\%$  vol for isotropic (blue/intermediate line) and aligned (green/upper line) fiber orientations. The addition of fibers leads to a substantial increase in the stress level along the jet and shifts the stress maximum to higher  $z$  values. This is easily explained by a larger viscosity of the mixture, which results to a steeper initial increase in the tensile stress and allows extension of the viscous regime to higher axial positions. Furthermore, the aligned fiber orientation promotes a higher extensional viscosity [23] and, consequently, the higher stress level in the jet than the isotropic orientation. For quantitative

**TABLE II.** Parameters of the CC-PA mixtures related to tensile stress calculations.

Fiber volume fraction/orientation	$\psi_S$	$\psi_E$	$z_m$ (mm)	$\sigma_{E,m}$ (Pa)
$\varphi_f = 0$ (no fibers)	N/A	N/A	53.4	143
$\varphi_f = 1\%$ vol (isotropic)	$\frac{1}{15}$	$\frac{1}{5}$	77.7	253
$\varphi_f = 1\%$ vol (aligned)	$\frac{0.315}{r_e} \approx 0.011^a$ , $r_e = \frac{1.24r}{\ln^{1/2}r}$	1	87.3	394

<sup>a</sup>The  $\psi_S$  parameter for the aligned orientation in a shear flow through the tube (from which the jet flows out) corresponds to the solution of Leal and Hinch [37] for the tumbling rods at vanishing Brownian or hydrodynamic rotary diffusivity.

comparison, the peak values of the tensile stress  $\sigma_{E,m}$  and corresponding axial position  $z_m$  are provided in Table II.

Increasing  $\sigma_{E,m}$  values with the addition of fibers presumably increases the stress range  $\Delta\sigma_E = \sigma_{E,m} - \sigma_{E,l}$  of the DST regime within the jet. However, the lower DST threshold stress in the CC-PA mixture is expected to increase with the fiber volume fraction that could reduce the DST interval  $\Delta\sigma_E$ . The increasing  $\sigma_{E,l}(\varphi_f)$ -dependency is expected to have a similar physics as the increasing  $\sigma_c(\varphi_f)$ -dependency revealed in shear flows [13]. As discussed in Sec. II B, this effect is related to local shear rates and local stress levels in the pores of the fiber network filled with a shear thickening matrix (CC suspension). This effect is captured semiquantitatively by the homogenization approach of Chateau *et al.* [38] extended to controlled stress shear rheology in Ref. [13]. Extrapolation to the axisymmetric extension within the jet is straightforward and gives the following expression for the lower DST threshold stress  $\sigma_{E,l}(\varphi_f)$  in the CC-PA mixture as a function of the DST threshold stress  $\sigma_{E,l}(0)$  in the CC matrix:

$$\sigma_{E,l}(\varphi_f) = \sigma_{E,l}(0) \sqrt{(1 - \varphi_f) \eta_{E,r}(\varphi_f)}. \quad (15)$$

It is important to stress that Eq. (15) is a mixture of three following theoretical models: (a) the WC model [5] capturing the DST transition in spherical particle suspensions; (b) the PTG model [35] developed for Newtonian fiber suspensions, and (c) the homogenization approach [38] developed for particle dispersions in non-Newtonian solvents. Such a combination needs justification. The WC model (typically applied to suspensions of spheres) is believed to apply to the sphere-fibers mixtures as long as the four following conditions are accomplished: (i) the size of CC particles is a few times smaller than the minor size (diameter) of PA fibers (scale separation condition); (ii) DST is generated in CC particles suspension (shear thickening matrix) filling the space between PA fibers; (iii) the fibers are added at concentrations below the percolation limit, so that they enhance the mixture viscosity but do not generate DST themselves; and (iv) there is no specific interactions between CC particles and PA fibers. At these conditions, verified in our experiments, both WC and PTG models can be extended to sphere-fiber mixtures upon appropriate rescaling of the shear rate and the shear stress, provided by the homogenization approach. In its original form, this approach postulates that the viscosity  $\eta$  of the mixture is equal to the product of the matrix viscosity  $\eta_m(\dot{\gamma}_{loc})$  evaluated at some local shear rate  $\dot{\gamma}_{loc}$  by the relative viscosity  $\eta_r$  of a fiber suspension dispersed in a Newtonian

solvent. This approach has been validated in literature through comparison with experimental results on suspensions of spherical or rod-like particles dispersed in different non-Newtonian suspending liquids [38–40]. In the present case of the controlled stress extensional flow, the matrix extensional viscosity  $\eta_{E,m}(\sigma_{E,loc})$  should be considered at a local tensile stress  $\sigma_{E,loc}$ , which results in Eq. (15) for the lower DST threshold.

To get quantitative evaluation of  $\sigma_{E,l}(\varphi_f)$ -dependency using Eq. (15), we need to know the lower DST threshold  $\sigma_{E,l}(0)$  of pure CC suspension. It can be evaluated from the minimal jet length,  $L_{min} \approx 60$  mm, above which the jet exhibits the lateral drift instability [Sec. III A 1]. In theory, the lower DST threshold corresponds to the stress level  $\sigma_E$  of the stress profile curve (red/lower line in Fig. 12) taken at  $z = L_{min}$ . In practice, we have to take into account fringing effects related to jet deceleration near the point where it hits the Petri dish. It seems more reasonable to replace the full jet length  $L_{min}$  by the axial distance  $L_{eff} \approx 35$  mm between the tube outlet and the point of the narrowest jet diameter. The lower DST threshold is then estimated to be about  $\sigma_{E,l}(0) = \sigma_E(z = L_{eff}) \approx 133$  Pa. We have to bear in mind that this is a very rough estimation subject to the uncertainty of the considered fringing effect and to possible errors of the theoretical evaluation of the stress profile. Injecting the  $\sigma_{E,l}(0)$ -value to Eq. (15), we are able to plot

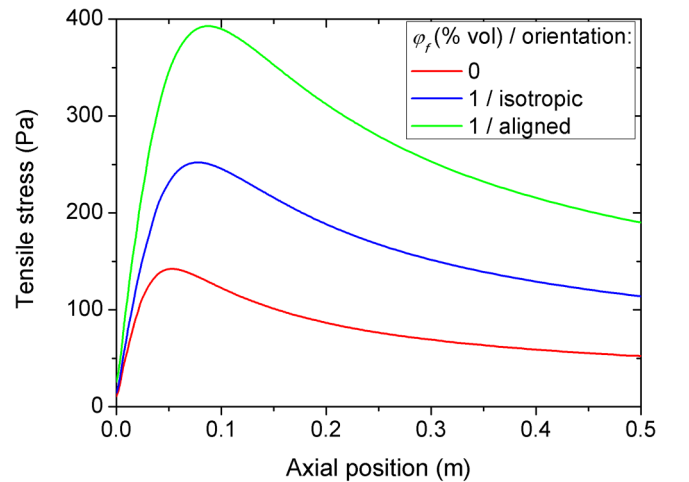


**FIG. 12.** Theoretical stress profiles along the jet in terms of tensile stress as a function of the axial position along the jet for CC suspension without fibers and CC-PA mixtures at  $\varphi_f = 1\%$  vol and two different fiber orientations.

$\sigma_{E,l}(\varphi_f)$ -dependency and compare it to previously evaluated  $\sigma_{E,m}(\varphi_f)$ -dependency for a particular case of isotropic fiber orientation—see Fig. 13(a).

Evaluation shows that the peak tensile stress  $\sigma_{E,m}(\varphi_f)$  exhibits a stronger increase with the fiber volume fraction compared to the lower DST threshold stress  $\sigma_{E,l}(\varphi_f)$ . This holds for the whole experimental range of  $\varphi_f$  and also for the aligned fiber orientation (curves not shown for brevity). This implies that, as already supposed, the stress range  $\Delta\sigma_E = \sigma_{E,m} - \sigma_{E,l}$  of the DST regime within the jet progressively increases with the fiber volume fraction. Thus, the fiber addition is expected to amplify jet lateral oscillations in contrast to experimental observations showing a full stabilization at  $\varphi_f \geq 0.8\%$  vol.

However, the DST regime can be bounded above by some upper DST threshold stress,  $\sigma_{E,u}$ , which is commonly ascribed to the capillary stress in the case of shear flows with the free surface [2] (as in plate-plate or cylindrical Couette geometries). In that case, through the frictional particle network, the applied shear stress induces a strong normal stress, which is no longer balanced by the ambient air pressure at the free surface but pushes the particles through the surface. The fluid menisci between poking particles at the free surface build a capillary pressure (stress), evaluated empirically as  $p_c \approx \gamma/D_c$ , with  $D_c$  being a characteristic size of the menisci between poking particles ( $D_c \approx 10D_p$  for spherical particles of a diameter  $D_p$ ). It has been experimentally confirmed that the applied shear stress,  $\sigma \approx p_c$ , corresponds to the end of the DST regime and the stress shows a modest increase with the shear rate above  $p_c$  [2]. Somewhat similar physics is supposed to hold in the present case of the extensional flow within the jet. The radial compressive stress  $\sigma_{rr}$  pushes the suspending liquid toward the jet centerline through a quasisolid particle frictional network; this can “bare” the peripheral particles at the jet surface and create menisci between them resulting in a strong capillary pressure. By analogy with shear flows with a free surface, the capillary pressure is expected to prevent particles from escaping the surface until the stress level in the suspension overcomes the characteristic capillary pressure. It is, therefore, reasonable to assign the capillary pressure to the upper DST threshold stress in extensional jet flows:  $\sigma_{E,u} \sim p_c \sim \gamma/D_c$ .

Since the fibers are much larger than the CC particles, the characteristic size  $D_c$  of the menisci is expected to be defined by some effective size of the fibers. This size should depend on their orientation and possibly the volume fraction and agglomeration state. Visual inspection of Fig. 4 reveals the appearance of short-scale ( $\lesssim 1$  mm) irregularities on the jet surface of CC-PA mixtures, different from blob-and-necks reported in Sec. III B 1 and having wavelengths  $\lambda \gtrsim 10$  mm. These irregularities seem to reflect poking of PA fibers through the jet surface; they are absent (or undistinguishable at current image resolution) for suspensions of CC particles without fibers and their sizes increase with the PA fiber volume fraction. This could be attributed to the existence of sparse fiber flocs whose size likely increases with the fiber volume fraction. Notice that formation of pulp fiber flocs within free jets of the papermaking furnish is a common phenomenon in the papermaking industry [41]. Unfortunately, space resolution of our CCD camera was too poor to get

reliable measurements of the floc size distribution. We can tentatively suppose that the floc size and consequently the characteristic menisci size  $D_c$  linearly increase with the fiber volume fraction  $D_c \propto \varphi_f$ , in qualitative agreement with pulp flocs behavior [41]. This leads to following semiempirical scaling for the upper DST threshold stress:

$$\sigma_{E,u} = \frac{\gamma}{D_{c,1}\varphi_f}, \quad (16)$$

where  $D_{c,1}$  is a size scale that should be determined from experiments. In practice, we can determine  $D_{c,1}$  by matching the lower and the upper DST thresholds at the fiber volume fraction  $\varphi_{f,c} \approx 0.75\%$  vol, above which the jet becomes stable. Equalizing the right-hand sides of Eqs. (15) and (16) at  $\varphi_f = \varphi_{f,c}$ , we get  $D_{c,1} \approx 63$  mm.

The upper DST threshold stress appears to be inversely proportional to the fiber volume fraction [Eq. (16)], as a direct consequence of our hypothesis on the characteristic size,  $D_c \propto \varphi_f$ . Of course, this scaling fails at very low fiber volume fractions  $\varphi_f \ll \varphi_{f,c} \approx 0.75\%$  vol when  $D_c$  expected to scale with CC particle size  $D_p \approx 5.5 \mu\text{m}$ . The semiempirical  $\sigma_{E,u}(\varphi_f)$ -dependency is shown in Fig. 13(a) by a red (decreasing) line. We see that the upper DST threshold stress  $\sigma_{E,u}(\varphi_f)$  becomes lower than the lower DST stress  $\sigma_{E,l}(\varphi_f)$  above a critical fiber volume fraction,  $\varphi_{f,c} \approx 0.75\%$  vol. Such a crossover means that DST cannot occur above  $\varphi_{f,c}$  that likely results in stable jets at  $\varphi_f > \varphi_{f,c}$  in agreement with experiments. Thus, the DST regime within the jet is bounded from above by either the peak tensile stress [black/upper increasing curve in Fig. 13(a)] or the upper DST threshold (red/decreasing curve) and is bounded from below by the lower DST threshold (blue/lower increasing curve). The hatched zone in Fig. 13(a) represents a DST region, which is likely equivalent to the region of jet instability against lateral oscillations. In this context, the whole Fig. 13(a) can be considered as a phase diagram of the jet stability, with the nonhatched region corresponding to stable jets.

Once the upper DST threshold is taken into account, the stress range of the DST regime within the jet can be evaluated as a vertical distance between the upper and lower bounds of the hatched zone in Fig. 13(a) giving the following expression:

$$\Delta\sigma_E(\varphi_f) = \begin{cases} \min(\sigma_{E,m}, \sigma_{E,u}) - \sigma_{E,l}, & \text{at } \varphi_f \lesssim \varphi_{f,c} \\ 0, & \text{at } \varphi_f \gtrsim \varphi_{f,c} \end{cases}. \quad (17)$$

It is quite intuitive to expect that the intensity of jet lateral oscillations at  $\varphi_f \lesssim \varphi_{f,c}$  is somehow correlated to the DST stress range  $\Delta\sigma_E$ . To check this point, we evaluated the RMS values of the lateral drift amplitude,  $x_{RMS}$ , and of the transverse jet speed,  $v_{RMS}$ , as adequate integral parameters describing the intensity of jet oscillations [cf. Sec. II C]. Notice that the kinetic energy (by unit jet volume) of lateral oscillations can be simply evaluated as  $e_{cin} = (1/2)\rho v_{RMS}^2 \cdot x_{RMS}(\varphi_f)$  and  $v_{RMS}(\varphi_f)$  experimental dependencies are shown in Fig. 13(b) compared with the theoretical

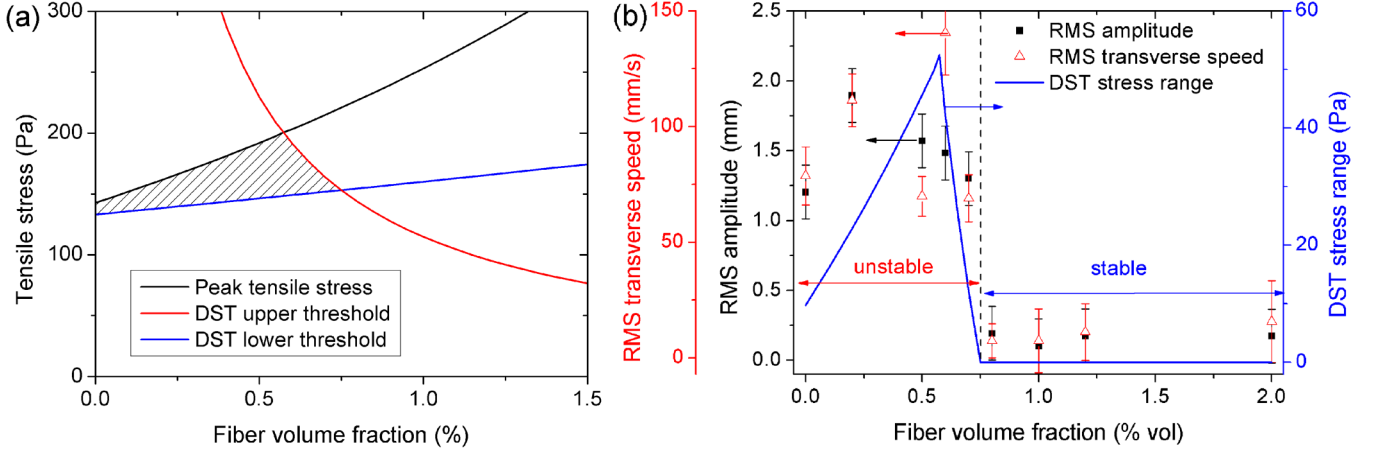


**FIG. 13.** Theoretical phase diagram of the jet stability with the hatched region indicating jet instability against lateral oscillations (DST regime) and nonhatched regions standing for stable jets (stable steady-state flow) (a). Experimental dependencies of the RMS amplitude and RMS transverse speed (left ordinate axes) on the fiber volume fraction compared to the semiempirical dependency of the DST stress range (right ordinate axis) on the fiber volume fraction (b).

$\Delta\sigma_E(\varphi_f)$ -dependency (blue line) with  $\Delta\sigma_E$  being assigned to the right ordinate axis. Both  $x_{RMS}$  and  $v_{RMS}$  seem to show an initial increase with the fiber volume fraction  $\varphi_f$  followed by a decrease and drastically fall at  $\varphi_f = 0.7 - 0.8\%$  vol, as the jet becomes visually stable. Figure 13(b) confirms that non-monotonic  $x_{RMS}(\varphi_f)$  and  $v_{RMS}(\varphi_f)$  dependencies correlate qualitatively with concentration dependency of the stress range  $\Delta\sigma_E(\varphi_f)$  of the DST regime. This is quite a logical issue: larger the DST stress interval, higher the intensity of jet lateral fluctuations. We consider it as another argument supporting the basic hypothesis on the rheological (DST) origin of the observed jet instability.

### 3. Break-up length

Jet stabilization above the critical fiber volume fraction still cannot explain why the jet breaks up at relatively short lengths without any transverse oscillation. To inspect this behavior, we evaluate the experimental break-up length,  $L_b$ , as the axial distance from the tube outlet above which the rupture probability in Fig. 5(b) departs from zero. The

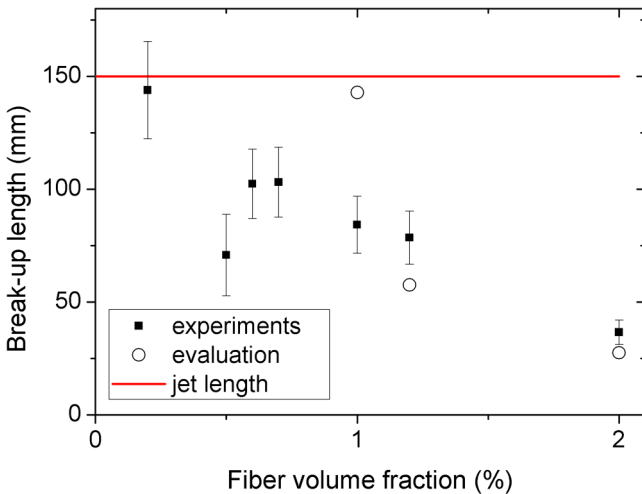


**FIG. 14.** Experimental and evaluated break-up length as a function of the fiber volume fraction. The red horizontal line stands for the jet length.

experimental  $L_b(\varphi_f)$ -dependency is plotted in Fig. 14 and confirms a progressive decrease in the rupture length with fiber volume fraction stated in Sec. III B 1.

First, we can compare our experimental  $L_b$ -values with the break-up length of RP instability. The gravity stretching of jets is known to considerably increase the break-up length and physically relevant expression for  $L_b$  has been provided by Javadi *et al.* [42]:  $L_b \approx 172(gu_0^2 R_0^4 \eta_0^4 / \gamma^4)^{1/3}$ , valid in the limit of high Ohnesorge numbers  $Oh = \eta_0(\rho\gamma R_0)^{-1/2} \gg 1$ , respected in our experiments. Taking into account the scaling  $u_0 \propto 1/\eta_0$  [Eq. (2)] for the jet velocity at the tube outlet, one finds  $L_b \propto \eta_0^{2/3}$  that contradicts to our observations of decreasing break-up length with increasing low-shear viscosity  $\eta_0$  of CC-PA mixtures at increasing fiber volume fractions. Quantitatively, the last expression gives the theoretical break-up length ranging between 300 and 430 mm, which is much larger than the experimental jet length  $L \approx 150$  mm. This discrepancy, along with the wave speed  $v_s \gg u$  [Sec. III B 2], allows us to definitely rule out the RP instability as a possible reason of the jet break-up.

A similar break-up is usually observed for the jet of Newtonian concentrated suspensions of spherical particles and is attributed to the finite size effect when the jet diameter thins under gravity up to a size equal to ten particle diameters [22]. The factor of 10 has been confirmed for several datasets at different particle diameters and suspending liquid viscosities. In our case of CC-PA mixtures, fibers are much larger than the CC particles, and the characteristic size  $D_c \propto \varphi_f$  of the fiber flocs is by far an appropriate scale of the jet diameter corresponding to the jet break-up. We can, therefore, determine the theoretical jet break-up length  $L_b$  as an axial position at which the jet average (over time) diameter is

$$\langle d \rangle = D_c = D_{c2}\varphi_f, \quad (18)$$

where  $D_{c2}$  is a size scale that should be determined from experiments. We evaluated the break-up length using experimental dependencies  $\langle d \rangle(z)$  of the jet average diameter on the axial distance [Fig. 5(a)]. Equalizing  $\langle d \rangle(z)$  from Fig. 5(a) to

the right-hand part of Eq. (18), we get semiempirical  $L_b$  values for each fiber volume fraction  $\varphi_f$  at different  $D_{c2}$  values. The final semiempirical  $L_b(\varphi_f)$ -dependency (corresponding to the finite particle size scenario of the jet break-up) is obtained by choosing a  $D_{c2}$  value that provides the closest agreement with the experimental  $L_b(\varphi_f)$  curve. This value is  $D_{c2} \approx 1$  mm under condition that  $\varphi_f$  in Eq. (18) is substituted in (% vol) units. Such evaluation gives discrete values of  $L_b$  at each experimental value of the fiber volume fraction. These discrete values are added to Fig. 14 as open circle symbols. We observe a qualitative agreement between experiments and evaluation, both showing the decrease in the break-up length with the fiber volume fraction that is ascribed to increasing critical jet diameter [Eq. (18)] corresponding to the jet rupture. Notice that at relatively weak fiber volume fractions  $\varphi_f \leq 0.7\%$  vol, the jet does not thin down the theoretical critical diameter [Eq. (18)], and the model does not predict jet rupture at  $\varphi_f \leq 0.7\%$  vol in contrast to experiments. This discrepancy is likely related to very rough evaluation of the fiber floc size  $D_c \propto \varphi_f$  whose scaling should be checked by recording of the jet flow at higher space resolution. At this stage, we can claim that an increasing size of jet surface roughness (fiber floc size) gives a good explanation for experimental concentration dependencies of the oscillation amplitude  $[x_{RMS}(\varphi_f)]$  and  $v_{RMS}(\varphi_f)$ , Fig. 13(b)] and break-up length  $[L_b(\varphi_f)]$ , Fig. 14].

#### IV. CONCLUSIONS

This work is devoted to the detailed study of the jet instability occurring in concentrated non-Brownian suspensions of different shaped particles presumably above DST transition in the extensional flow. In experiments, we employed either an aqueous suspension of CC isotropic-shaped particles coated with a polymer brush or aqueous mixtures of CC particles with PA fibers at CC and PA volume fractions, respectively,  $\varphi_p = \text{const} = 68\%$  vol and  $\varphi_f = 0\% - 2\%$  vol, with PA aspect ratio  $r \approx 47$ . The jets of these fluids were subjected to a free fall under gravitational stretching at a constant flow rate. The jets were filmed with a high-speed camera and the stacks of the frames were processed with MATLAB software in order to extract several quantitative characteristics of the jet dynamics. Evaluations of the tensile stress profile along the jet allowed us to shed more light to the origin of the observed instability and to propose explanations of the effect of fiber addition on observed oscillation-to-break-up transition. The main results can be summarized as follows:

(1) In the absence of PA fibers, direct visualization of falling jets of CC suspension reveals relatively strong lateral oscillations occurring for jet lengths  $L \gtrsim 6$  cm. Spatiotemporal diagrams show that the jet lateral drift  $x(t, z)$  is accompanied by small but distinguishable undulations  $\Delta d(t, z)$  of the jet diameter. The 2D DFT analysis of  $x(t, z)$  and  $\Delta d(t, z)$  reveals approximately linear dispersion relations for propagation of lateral oscillations ( $\omega \approx v_l k$ ) and diameter undulation ( $\omega \approx v_s k$ ) reminiscent for nondispersive waves. The wave speeds are (within experimental errors) similar for both wave types,  $v_l \approx v_s \approx 0.9$  m/s, being

much larger than the jet speed. Moreover, both  $x(t, z)$  and  $\Delta d(t, z)$  oscillations are observed within nearly similar wavelength range  $\lambda \sim 0.01 - 0.15$  m bounded above by the jet length. This allows supposing both wave types to be of the same origin related to stress fluctuations above DST transition, while the Rayleigh-Plateau instability for  $\Delta d(t, z)$  is ruled out. The difference is that the diameter undulation propagates only downstream the jet, while the lateral oscillations propagate both downstream at  $v_l \approx 0.9$  m/s and upstream at  $v_l \approx -0.9$  m/s. The lateral drift Fourier amplitude (wave crest height)  $X_c$  decreases with the wave crest length  $L_c \propto \omega \propto k$ , with the dominant wavelength being equal to the jet length.

- (2) Adapting the WC model [5] to extensional flows, we predict abrupt (but mathematically continuous) increase in the tensile stress  $\sigma_E$  along the jet at a location corresponding to the lower threshold stress  $\sigma_{E,l}$  of DST transition. Such a tensile stress jump is believed to be responsible for jet instability by analogy with shock wave behaviors [34]. Above DST transition, tensile stress fluctuations are expected to lead to fluctuation of the longitudinal and transverse velocity fields within the jet; the former being manifested through undulation of the jet diameter and the latter being perceived as jet transverse oscillations. Hence, linear and nonlinear stability analyses are required to validate these hypotheses.
- (3) Addition of PA fibers to CC suspension damps lateral oscillations at fiber volume fraction  $\varphi_f \gtrsim 0.75\%$  vol but favors ruptures along the jet at a critical break-up length  $L_b$  decreasing with  $\varphi_f$ . Such oscillation-to-break up transition is tentatively explained by the interplay between growing lower ( $\sigma_{E,l}$ ) and decreasing upper ( $\sigma_{E,u}$ ) DST threshold stress with increasing  $\varphi_f$  along with the jet thinning down the size of fiber flocs poking through the jet surface when the tensile stress overcomes the capillary pressure. The upper concentration limit,  $\varphi_{f,c} \approx 0.75\%$  vol, of jet instability is fixed by the crossover of the two DST thresholds  $\sigma_{E,l}$  and  $\sigma_{E,u}$ . The lower concentration limit is simply  $\varphi_f = 0$  for any jet length  $L \gtrsim 60$  mm because the tensile stress  $\sigma_E$  along the jet overcomes the lower DST threshold stress  $\sigma_{E,l}$  at  $\varphi_f = 0$ . Our theoretical model allows plotting a  $(\sigma_E, \varphi_f)$  phase diagram of jet stability and qualitatively captures the shapes of concentration dependencies of the break-up length  $L_b(\varphi_f)$ , RMS oscillation amplitude  $x_{RMS}(\varphi_f)$ , and RMS transverse speed  $v_{RMS}(\varphi_f)$ . On the other hand, within statistical errors, the wave speeds are poorly affected by the addition of fibers. This agrees with the model of vibrating solid string under gravitational stretching predicting the wave speed  $v_l = \sqrt{gL/2}$  independent of any rheological parameters including the particle volume fraction. Surprisingly, experimental wave speed values  $v_l = 0.9 \pm 0.2$  m/s are in good quantitative agreement with the vibrating string model,  $v_l \approx 0.87$  m/s, as already reported by Liard *et al.* [19]. Such agreement likely suggests solid-like behavior of the unstable jet above DST transition.
- (4) Because of jet opacity, we were unable to establish the effect of fiber orientation on jet behavior. However, from evaluations of  $\sigma_E(z)$  and  $\sigma_{E,l}(\varphi_f)$ , we could anticipate

that the flow-aligned fibers provide distinguishable increase in the peak stress  $\sigma_{E,m}$  and the lower DST threshold  $\sigma_{E,l}$  with respect to random orientation. However, random orientation better correlates with the particle poking scenario of the upper DST threshold and jet break-up (the fibers aligned along the jet surface would not result in significant jet surface “roughness” observed in experiments). In addition to it, in our previous study, the random fiber orientation gave better flow curve predictions in shear flows as compared to aligned orientation [13].

The results of this work are believed to be useful for both practical applications of shear thickening jets (in cement jet grouting, shear thickening polishing, abrasive jet cutting, mortar spraying, cement pumping, etc.) and academic research through detailed characterization of the new type of jet instability and alternative testing of extensional rheology of DST fluids. In fact, one can measure the radius profile along the jet,  $R(z)$ ; then, rearranging/integrating Eqs. (7a)–(7c), it is possible to express the extension rate and tensile stress as a function of the axial coordinate  $z$ ; so the flow curve  $\sigma_E = f(\dot{\epsilon})$  can be plotted in a parametric form  $[\dot{\epsilon}(z); \sigma_E(z)]$ , with  $z$  being a parameter. A separate study is needed to develop this rheometric method.

## ACKNOWLEDGMENTS

The authors acknowledge French “Agence Nationale de la Recherche” (Project Future Investments UCA JEDI, No. ANR-15-IDEX-01, project “RheoCimPI”) for financial support. M.M. acknowledges the PROFAS B+ Program for his Ph.D. grant funding. The authors are grateful to F. Celestini and G. Bossis (UCA, INPHYNI, Nice) for helpful discussions and to P. Boustingorry (CHRYSO, France) for providing us with the superplasticizer.

## AUTHOR DECLARATIONS

### Conflict of Interest

The authors have no conflicts to disclose.

## REFERENCES

- [1] Eggers, J., and E. Villermaux, “Physics of liquid jets,” *Rep. Prog. Phys.* **71**(3), 036601 (2008).
- [2] Brown, E., and H. M. Jaeger, “Shear thickening in concentrated suspensions: Phenomenology, mechanisms and relations to jamming,” *Rep. Prog. Phys.* **77**(4), 046602 (2014).
- [3] Denn, M. M., J. F. Morris, and D. Bonn, “Shear thickening in concentrated suspensions of smooth spheres in newtonian suspending fluids,” *Soft Matter* **14**(2), 170–184 (2018).
- [4] Seto, R., R. Mari, J. F. Morris, and M. M. Denn, “Discontinuous shear thickening of frictional hard-sphere suspensions,” *Phys. Rev. Lett.* **111**(21), 1–5 (2013).
- [5] Wyart, M., and M. E. Cates, “Discontinuous shear thickening without inertia in dense non-Brownian suspensions,” *Phys. Rev. Lett.* **112**(9), 1–5 (2014).
- [6] Ozturk, D., M. L. Morgan, and B. Sandnes, “Flow-to-fracture transition and pattern formation in a discontinuous shear thickening fluid,” *Commun. Phys.* **3**(1), 1–9 (2020).
- [7] Hermes, M., B. M. Guy, W. C. K. Poon, G. Poy, M. E. Cates, and M. Wyart, “Unsteady flow and particle migration in dense, non-Brownian suspensions,” *J. Rheol.* **60**(5), 905–916 (2016).
- [8] Chacko, R. N., R. Mari, M. E. Cates, and S. M. Fielding, “Dynamic vorticity banding in discontinuously shear thickening suspensions,” *Phys. Rev. Lett.* **121**(10), 108003 (2018).
- [9] Singh, A., S. Pednekar, J. Chun, M. M. Denn, and J. F. Morris, “From yielding to shear jamming in a cohesive frictional suspension,” *Phys. Rev. Lett.* **122**(9), 098004 (2019).
- [10] Bossis, G., P. Boustingorry, Y. Grasselli, A. Meunier, R. Morini, A. Zubarev, and O. Volkova, “Discontinuous shear thickening in the presence of polymers adsorbed on the surface of calcium carbonate particles,” *Rheol. Acta* **56**(5), 415–430 (2017).
- [11] Comtet, J., G. Chatté, A. Niguès, L. Bocquet, A. Siria, and A. Colin, “Pairwise frictional profile between particles determines discontinuous shear thickening transition in non-colloidal suspensions,” *Nat. Commun.* **8**(1), 1–7 (2017).
- [12] Brown, E., H. Zhang, N. A. Forman, B. W. Maynor, D. E. Betts, J. M. DeSimone, and H. M. Jaeger, “Shear thickening and jamming in densely packed suspensions of different particle shapes,” *Phys. Rev. E* **84**(3), 031408 (2011).
- [13] Sidaoui, N., P. Arenas Fernandez, G. Bossis, O. Volkova, M. Meloussi, S. Aguib, and P. Kuzhir, “Discontinuous shear thickening in concentrated mixtures of isotropic-shaped and rod-like particles tested through mixer type rheometry,” *J. Rheol.* **64**(4), 817–836 (2020).
- [14] Bischoff White, E. E., M. Chellamuthu, and J. P. Rothstein, “Extensional rheology of a shear-thickening cornstarch and water suspension,” *Rheol. Acta* **49**(2), 119–129 (2010).
- [15] Andrade, R. J. E., A. R. Jacob, F. J. Galindo-Rosales, L. Campo-Deaño, Q. Huang, O. Hassager, and G. Petekidis, “Dilatancy in dense suspensions of model hard-sphere-like colloids under shear and extensional flow,” *J. Rheol.* **64**(5), 1179–1196 (2020).
- [16] Roché, M., H. Kellay, and H. A. Stone, “Heterogeneity and the role of normal stresses during the extensional thinning of non-Brownian shear-thickening fluids,” *Phys. Rev. Lett.* **107**(13), 134503 (2011).
- [17] Seto, R., G. G. Giusteri, and A. Martiniello, “Microstructure and thickening of dense suspensions under extensional and shear flows,” *J. Fluid Mech.* **825**, R3 (2017).
- [18] Darbois Texier, B., H. Lhuissier, Y. Forterre, and B. Metzger, “Surface-wave instability without inertia in shear-thickening suspensions,” *Commun. Phys.* **3**(1), 1–7 (2020).
- [19] Liard, M., A. Sato, J. Sautel, D. Lootens, and P. Hébraud, “Jet instability of a shear-thickening concentrated suspension,” *Eur. Phys. J. E* **43**, 69 (2020).
- [20] Wang, Z. Y., H. Zhao, W. F. Li, J. L. Xu, and H. F. Liu, “Primary breakup of shear-thickening suspension jet by an annular air jet,” *AICHE J.* **68**(4), e17579 (2022).
- [21] Wang, Z.-Y., H. Zhao, W.-F. Li, J.-L. Xu, and H.-F. Liu, “Secondary breakup of shear thickening suspension drop,” *Phys. Fluids* **33**(9), 093103 (2021).
- [22] Château, J., and H. Lhuissier, “Breakup of a particulate suspension jet,” *Phys. Rev. Fluids* **4**(1), 012001(R) (2019).
- [23] Macosko, C. W., *Rheology Principles, Measurements, and Applications* (Wiley-VCH, New York, 1994).
- [24] Becker, L. E., and M. J. Shelley, “Instability of elastic filaments in shear flow yields first-normal-stress differences,” *Phys. Rev. Lett.* **87**(19), 198301 (2001).

- [25] Bounoua, S. N., P. Kuzhir, and E. Lemaire, "Shear reversal experiments on concentrated rigid fiber suspensions," *J. Rheol.* **63**(5), 785–798 (2019).
- [26] Morini, R., Rheology of concentrated suspensions of calcium carbonate in the presence of superplasticizer, Ph.D. thesis, University of Nice-Sophia Antipolis, 2013, (in French).
- [27] Ianni, F., D. Lasne, R. Sarcia, and P. Hébraud, "Relaxation of jammed colloidal suspensions after shear cessation," *Phys. Rev. E* **74**(1), 1–6 (2006).
- [28] See supplementary material with four movies of the falling jets: each movie corresponds to the snapshots of Fig. 4 and is named accordingly (Fig4a.avi, ..., Fig4d.avi). The videos are best played using the VLC media player.
- [29] Senchenko, S., and T. Bohr, "Shape and stability of a viscous thread," *Phys. Rev. E* **71**(5), 056301 (2005).
- [30] Koenders, M. A. C., "Wave propagation through elastic granular and granular auxetic materials," *Phys. Status Solidi B* **246**(9), 2083–2088 (2009).
- [31] Puri, P., and S. C. Cowin, "Plane waves in linear elastic materials with voids," *J. Elasticity* **15**(2), 167–183 (1985).
- [32] Hou, Z., R. J. Okamoto, and P. V. Bayly, "Shear wave propagation and estimation of material parameters in a nonlinear, fibrous material," *J. Biomech. Eng.* **142**(5), 051010 (2020).
- [33] Sauter, U. S., and H. W. Buggisch, "Stability of initially slow viscous jets driven by gravity," *J. Fluid Mech.* **533**, 237–257 (2005).
- [34] Landau, L. D., and E. M. Lifshitz, *A Course in Theoretical Physics—Fluid Mechanics* (Pergamon, New York, 1987), Vol. 6.
- [35] Phan-Thien, N., and A. L. Graham, "A new constitutive model for fibre suspensions: Flow past a sphere," *Rheol. Acta* **30**(1), 44–57 (1991).
- [36] Solomon, M. J., and P. T. Spicer, "Microstructural regimes of colloidal rod suspensions, gels, and glasses," *Soft Matter* **6**(7), 1391–1400 (2010).
- [37] Leal, L. G., and E. J. Hinch, "The effect of weak Brownian rotations on particles in shear flow," *J. Fluid Mech.* **46**(4), 685–703 (1971).
- [38] Chateau, X., G. Ovarlez, and K. L. Trung, "Homogenization approach to the behavior of suspensions of noncolloidal particles in yield stress fluids," *J. Rheol.* **52**(2), 489–506 (2008).
- [39] Ovarlez, G., F. Mahaut, S. Deboeuf, N. Lenoir, S. Hormozi, and X. Chateau, "Flows of suspensions of particles in yield stress fluids," *J. Rheol.* **59**(6), 1449–1486 (2015).
- [40] Marins, J. A., T. Plachý, and P. Kuzhir, "Iron–sepiolite magnetorheological fluids with improved performances," *J. Rheol.* **63**(1), 125–139 (2019).
- [41] Hubbe, M. A., "Flocculation and redispersion of cellulosic fiber suspensions: A review of effects of hydrodynamic shear and polyelectrolytes," *BioResources* **2**(2), 296–331 (2007).
- [42] Javadi, A., J. Eggers, D. Bonn, M. Habibi, and N. M. Ribe, "Delayed capillary breakup of falling viscous jets," *Phys. Rev. Lett.* **110**(14), 144501 (2013).